AIMS Mathematics

http://www.aimspress.com/journal/Math

AIMS Mathematics, 10(10): 24923–24957.
DOI: 10.3934/math.20251103
Received: 17 July 2025
Revised: 19 October 2025
Accepted: 21 October 2025
Published: 30 October 2025

Research article

An epidemiological model of the mumps virus via Mittag-Leffler Kernel: Stability analysis and artificial neural network solutions

I-Hung Lee[1], **Sanaullah Saqib**[1], **Qin Sheng**[2] **and Yin-Tzer Shih**[1,*]

[1] Department of Applied Mathematics, National Chung Hsing University, Taichung 402202, Taiwan
[2] Department of Mathematics and Center for Astrophysics, Space Physics and Engineering Research, Baylor University, Waco, TX 76798-7328, USA

* **Correspondence:** Email: yintzer_shih@email.nchu.edu.tw; Tel: +886422853459.

Abstract: This study presents a mathematical model utilizing fractal fractional-order Mittag-Leffler (FFM) operators to investigate the transmission dynamics of the mumps virus. The model was assessed both qualitatively and quantitatively, focusing on the existence and uniqueness of solutions, Ulam-Hyers stability, well-posedness, and treatment sensitivity analysis related to the Paramyxoviridae family. Fixed-point theory was used to establish solution constraints for modeling fractional dynamics. A comparative analysis revealed that the fractional-order model outperforms traditional integer-order approaches, offering a more robust and realistic framework for studying mumps virus epidemiology. Synthetic data generated from the two-step Newton solver with a Mittag-Leffler kernel was analyzed using supervised learning techniques and artificial neural networks. The neural network predictions closely matched the numerical results, showing minimal errors, and were validated through convergence metrics and regression analysis. This integrated framework offers a strong method for understanding the transmission dynamics of the mumps virus.

Keywords: mumps virus model; Mittage-Leffler Kernel; sensitivity; solution uniqueness; Ulam-Hyres stability; artificial neural network
Mathematics Subject Classification: 26A33, 34A08, 34A34, 65L20, 92B20, 92D30

---

1. Introduction

Hearing loss is a significant global health issue characterized by a partial or complete inability to hear due to abnormalities in the auditory system. According to the World Health Organization (WHO), over 430 million people worldwide are affected, including about 34 million children [1]. Hearing loss presents various symptoms, such as difficulty hearing in noisy environments, hypersensitivity to certain sounds, and trouble participating in everyday conversations. Its causes are diverse, ranging from genetic mutations and congenital disorders to traumatic injuries and viral infections impacting the outer, middle, or inner ear. Systemic conditions like diabetes mellitus and hypertension, along with environmental factors such as sudden or prolonged noise exposure, also play a significant role. Notably, noise-induced hearing loss is becoming increasingly common among younger populations, primarily due to the widespread use of personal music devices. This condition can cause irreversible damage to cochlear hair cells, which, in mammals, lack regenerative capacity . Mathematical modeling and data-driven simulations are crucial for developing effective prevention strategies and understanding the progression of hearing loss [2–7].

In recent decades, researchers worldwide have made significant progress in using numerical methods to clarify complex processes and phenomena, thereby improving our understanding of dynamic systems [8–11]. The emergence of fractional-order derivatives has introduced a new way to model natural processes, capturing their inherent nonlocal and memory-dependent characteristics [4, 5, 12]. Notably, advances in fractal-fractional models for infectious diseases, especially those incorporating the Mittag-Leffler kernel, can be found in [6, 7, 13, 14]. This study presents a novel mathematical model for hearing loss associated with the mumps virus, employing fractional-order approximations based on the Mittag-Leffler derivative. The analysis emphasizes the basic reproduction number, a key epidemiological metric that determines whether the disease will spread or decline. By examining how various parameters affect the reproduction number, the study aims to identify crucial factors for effective disease control. Artificial neural networks (ANNs) will be used to effectively manage the nonlinear, multidimensional complexities of the systems that emerge.

The following highlights describe our research:

- This study aims to use nonlinear autoregressive exogenous (NARX) networks to analyze the dynamics of mathematical models related to the epidemiological research of mumps virus transmission, with comparative insights from measles models.
- Synthetic data are created using Newton's two-step method, customized for the mumps viral model. Predictions are generated through a supervised learning approach using ANNs. The results consistently match numerical simulations across all model variations, showing minimal error and confirming the reliability of the proposed framework.
- Error distributions, illustrated through histograms, along with controlled measures optimizing iterative convergence based on mean squared error and regression outcomes, effectively demonstrate the strong performance of the proposed ANN approach in the epidemiological analysis of the mumps viral model. Qualitative and quantitative analyses of the fractional-order model are provided.
- Key well-posedness features of the fractional-order model for mumps viral infection, including the existence and uniqueness of solutions and the characterization of disease-free equilibrium points, are thoroughly established.
- A sensitivity analysis of the FFM fractional mumps model with therapeutic intervention is performed. Both local and global dynamics of mumps virus infection are evaluated through Ulam-Hyers (UH) stability analysis.
- In this paper, we present approximate solutions for various fractional orders when $R_0 < 1$. The results show that as the fractional order increases, $L(t)$ decreases, while $S(t)$ and $R(t)$ increase as the fractional order decreases. In all cases, the system approaches a steady state as the fractional order is lowered, indicating that the model yields more accurate results with a fractional order

lower than that of the classical (integer-order) derivative.

- Furthermore, we present estimated solutions for various fractional orders when $R_0 < 1$. The results show that $S(t)$ and $R(t)$ decrease as the fractional order decreases, while $L(t)$ increases with higher fractional values. Additionally, all trajectories tend toward a steady state as the fractional order is lowered, indicating improved solution behavior when the fractional order is below that of the classical derivative. Each compartment demonstrates convergent behavior and maintains its relative dynamics over time, accurately reflecting the progression of mumps viral infection.

This paper is organized as follows: Section 1 introduces a general framework for fractional-order modeling. Section 2 investigates fundamental fractional-order derivatives relevant to epidemiological virus transmission, laying the groundwork for an updated model formulation and analysis of the FFM model. Section 3 presents a standard well-posedness analysis of the proposed model, including discussions on solution existence and uniqueness, sensitivity analysis, and the disease-free equilibrium. Section 4 explores UH stability and provides a rigorous stability analysis of the model. Section 5 examines the discretized numerical scheme developed using the Mittag-Leffler kernel. Section 6 is devoted to comprehensive computational simulations. Section 7 discusses the application of ANN procedures and the resulting implementation outcomes for modeling the dynamics of mumps viral infection. Finally, Section 9 offers concluding remarks and outlines directions for continuing explorations.

2. Mathematical fractional model for hearing impairment

To begin, we need several fundamental results and dynamic properties from fractional calculus that are essential for the development of our model [15].

Definition 2.1. [15] *Let $\psi(t)$ be continuous for $t \in (0,T)$ for $T > 0$, and define the Mittag-Leffler kernel function*

$$\mathrm{E}_{\upsilon_1}(x) = \sum_{i=0}^{\infty} \frac{x^i}{\Gamma(i\upsilon_1 + 1)}, \quad \text{for } \upsilon_1 > 0.$$

The fractal fractional derivative of $\psi(t)$ of order υ_1 with the Mittag-Leffler kernel in the fractal dimension υ_2 is expressed by

$$^{FFM}\mathbb{D}_{0,t}^{\upsilon_1,\upsilon_2}\psi(t) = \frac{H(\upsilon_1)}{(1-\upsilon_1)}\frac{d^{\upsilon_2}}{dt^{\upsilon_2}}\int_0^t \mathrm{E}_{\upsilon_1}\left(-\frac{\upsilon_1(t-\rho)^{\upsilon_1}}{1-\upsilon_1}\right)\psi(\rho)d\rho, \tag{2.1}$$

where $H(\upsilon_1)$ is a normalization function with $H(0) = H(1) = 1,\ 0 \le \upsilon_1 < 1$, and $0 < \upsilon_2 \le 1$.

Further, a fractal fractional integral of $\psi(t)$ of order υ_1 with the Mittag-Leffier kernel is

$$^{FFM}\mathbb{I}_{0,t}^{\upsilon_1,\upsilon_2}\psi(t) = \frac{(1-\upsilon_1)t^{1-\upsilon_2}\psi(t)}{H(\upsilon_1)} + \frac{\upsilon_1}{H(\upsilon_1)\Gamma(\upsilon_1)}\int_0^t \rho^{1-\upsilon_2}(t-\rho)^{\upsilon_1-1}\psi(\rho)d\rho. \tag{2.2}$$

We now introduce an empirically compartmentalized model to describe the transmission dynamics of the mumps virus. To contextualize this framework, we refer to the compartmental epidemic model developed by Mohammadi et al. [16], which helps clarify key transmission mechanisms and notable features of viral spread. The dynamics of the mumps epidemic, including the effects of treatment interventions, are governed by the following system of nonlinear ordinary differential equations:

$$\begin{cases} {}^{FFM}\mathbb{D}_{0,t}^{\upsilon_1,\upsilon_2}S = \omega - \delta LS - \gamma S, \\ {}^{FFM}\mathbb{D}_{0,t}^{\upsilon_1,\upsilon_2}L = \delta LS - (\gamma + \tau)L, \\ {}^{FFM}\mathbb{D}_{0,t}^{\upsilon_1,\upsilon_2}R = L\tau - R\gamma, \end{cases} \tag{2.3}$$

together with initial conditions

$$S(0) = S^0 \geq 0, L(0) = L^0 \geq 0, R(0) = R^0 \geq 0, \tag{2.4}$$

where ω is the rate of population recruitment, δ is the rate at which the mumps virus spreads, γ is the natural death rate of the population, and τ is the recovery rate for infectious individuals.

The proposed fractional-order SIR model is developed to address the treatment and control of the mumps virus infection, incorporating the influence of high-capacity individuals and considering three distinct population compartments. Specifically, $S(t)$ indicates the susceptible population at time t, $L(t)$ represents the infected population, and $R(t)$ corresponds to the recovered population. Therefore, the total population at time t is denoted by $\mathbb{N}(t)$, and

$$\mathbb{N}(t) = S(t) + L(t) + R(t), \quad t \geq 0. \tag{2.5}$$

3. Well-posedness of the model and its qualitative analysis

This section explores the period and domain in which the outcomes of our framework hold meaningful historical significance. Throughout the analysis, we assume that all model variables and parameters remain positive for all values of $t \geq 0$. Therefore,

$${}^{FFM}\mathbb{D}_{0,t}^{\upsilon_1,\upsilon_2}\mathbb{N}(t) = -\gamma\mathbb{N}(t), \quad t > 0. \tag{3.1}$$

Since we expect $\mathbb{N}(t)$ to be positively increasing, thus,

$${}^{FFM}\mathbb{D}_{0,t}^{\upsilon_1,\upsilon_2}\mathbb{N}(t) > 0, \;\; {}^{FFM}\mathbb{D}_{0,t}^{\upsilon_1,\upsilon_2}\mathbb{N}(t) \geq \mathbb{N}(t), \;\; \text{and} \;\; {}^{FFM}\mathbb{D}_{0,t}^{\upsilon_1,\upsilon_2}\mathbb{N}(t) < \frac{1}{\gamma}. \tag{3.2}$$

The inequalities in (3.2) represent a threshold population level in the study. Consequently, the set of solutions to (2.3) should be restricted to

$$\Omega = \left\{(S, L, R) \in \mathbb{R}_+^3 : S + L + R < \frac{1}{\gamma}\right\}. \tag{3.3}$$

Here, $\mathbb{R}_+^3$ refers to a positive cone in $\mathbb{R}^3$, which also includes its lower-dimensional faces. To maintain proper realism, we exclude the scenario where ${}^{FFM}\mathbb{D}_{0,t}^{\upsilon_1,\upsilon_2}\mathbb{N}(t) \geq 0$, as it may imply that the host population may simultaneously decline to the carrying capacity.

The system of nonlinear differential equations (2.3) is designed to enhance our understanding of the fundamental dynamics governing mumps transmission and the influence of various parameters on these processes. Therefore, a comprehensive qualitative analysis of this mathematical model, including treatment interventions, is essential. Such an analysis will not only deepen insights into disease transmission dynamics but also help identify critical thresholds, such as the basic reproduction number, which determines the potential for outbreaks. Furthermore, evaluating the model's sensitivity to parameters such as treatment efficacy and transmission rates can inform the development of targeted strategies to control the spread of the virus and optimize resource allocation in public health. By integrating mathematical rigor with epidemiological relevance, this study contributes to the advancement of more effective and informed control measures for mumps.

3.1. Disease-free equilibrium

The disease-free equilibrium of the model system (2.3) may be obtained by setting

$$^{FFM}\mathbb{D}_{0,t}^{\upsilon_1,\upsilon_2}S(t) \;=\; ^{FFM}\mathbb{D}_{0,t}^{\upsilon_1,\upsilon_2}L(t) \;=\; ^{FFM}\mathbb{D}_{0,t}^{\upsilon_1,\upsilon_2}R(t) = 0, \quad t > 0,$$

as outlined in [16]. The above interprets that the equilibrium conditions are

$$S = \frac{\omega}{\gamma}, \;\; L = 0, \;\; R = 0. \tag{3.4}$$

3.2. Sensitivity analysis

The reproductive number R_0 can be expressed as [16]

$$R_0 = \frac{\omega\delta}{(\gamma+\tau)\gamma}. \tag{3.5}$$

The sensitivity of the virus reproduction can thus be evaluated through

$$\begin{aligned}
\frac{\partial R_0}{\partial \omega} &= \frac{\delta}{(\gamma+\tau)\gamma} > 0,\\
\frac{\partial R_0}{\partial \delta} &= \frac{\omega}{(\gamma+\tau)\gamma} > 0,\\
\frac{\partial R_0}{\partial \tau} &= -\frac{\omega\delta}{\gamma(\tau+\gamma)^2} < 0,\\
\frac{\partial R_0}{\partial \gamma} &= -\frac{\omega\delta(2\gamma+\tau)}{(\gamma+\tau)^2\gamma^2} < 0.
\end{aligned}$$

In this study, parameters ω and δ exhibit increasing trends, while γ and τ show decreasing trends. The sensitivity analysis results indicate that prevention remains the most effective strategy for controlling the disease. Given the specified parameter values, we find that $R_0 = 0.9976958 < 1$, indicating that under these conditions, the disease is unlikely to spread widely.

Figure 1 shows that R_0 is highly sensitive to variations in parameter values. The results of the sensitivity analysis suggest that prevention remains the most effective strategy for controlling the disease.

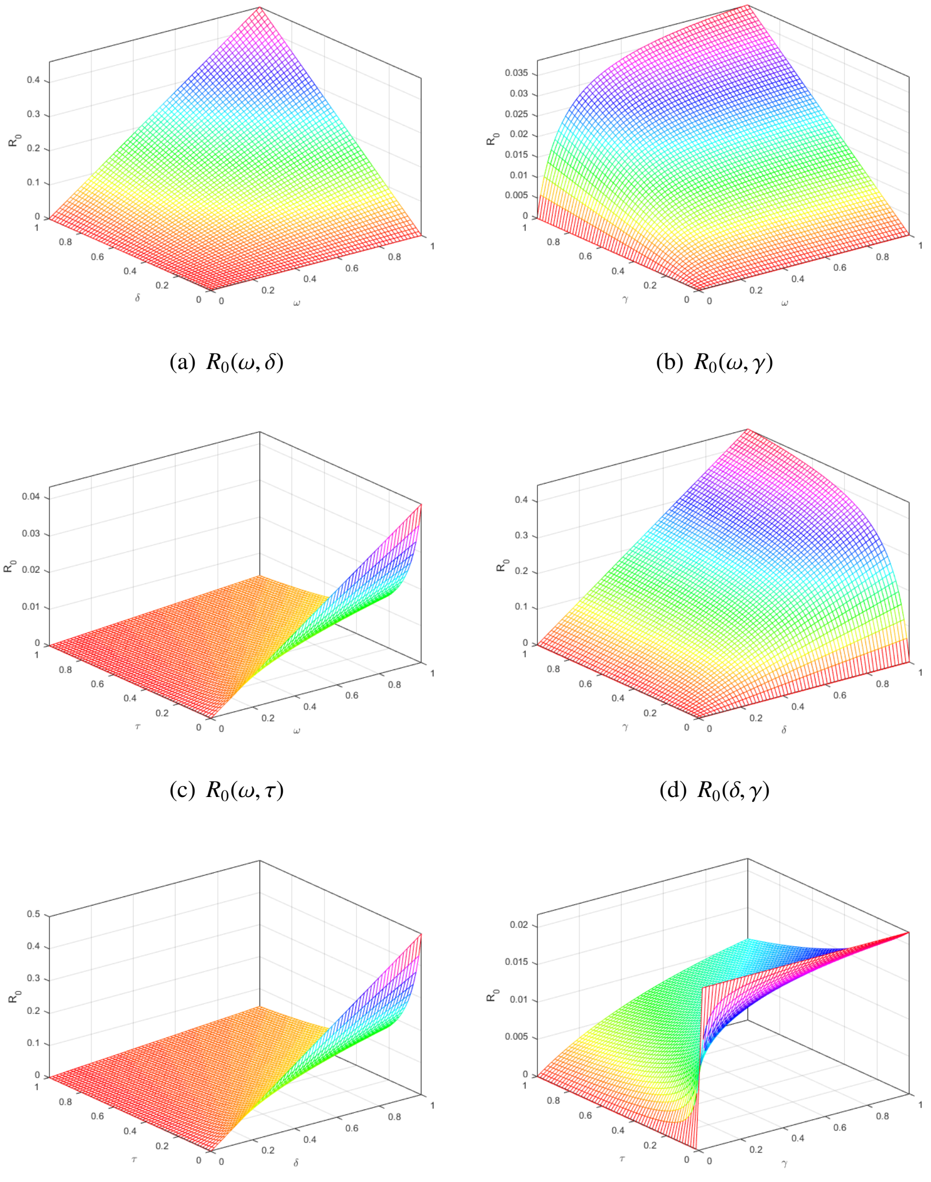

(a) $R_0(\omega, \delta)$ (b) $R_0(\omega, \gamma)$

(c) $R_0(\omega, \tau)$ (d) $R_0(\delta, \gamma)$

(e) $R_0(\delta, \tau)$ (f) $R_0(\gamma, \tau)$

Figure 1. A three-dimensional visualization of the basic reproduction number R_0 as a function of multiple parameter variations.

R_0 increases with positive sensitivity indices and decreases with negative indices. The research highlights key factors that influence transmission potential, enabling the identification of critical variables and their implications for the spread of pink eye. Variations in the parameter significantly affect R_0. Tables 1–2 and Figures 2–3 represent the sensitivity of various parameters for Scenario 1 ($R_0 < 1$) and Scenario 2 ($R_0 > 1$).

Table 1. The sensitivity index of the suggested paradigm for $R_0 < 1$.

Parameters	Sensitivity index	Index values
ω	$\Theta_{\omega}^{R_0}$	1.9954
δ	$\Theta_{\delta}^{R_0}$	23.0415
τ	$\Theta_{\tau}^{R_0}$	-4.5977
γ	$\Theta_{\gamma}^{R_0}$	-14.5746

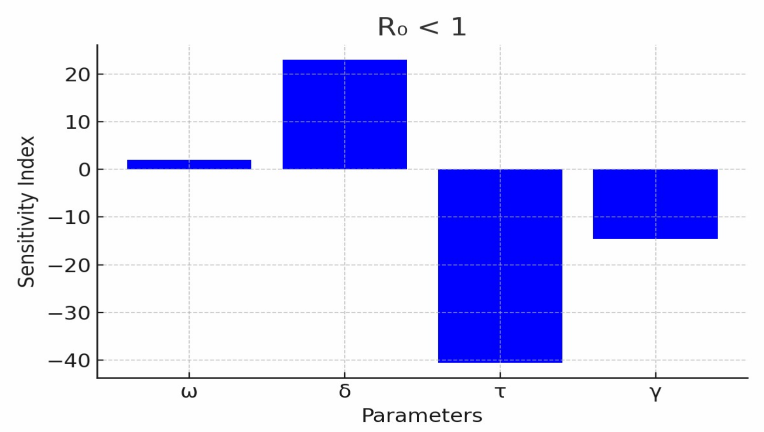

Figure 2. Sensitivity analysis of model parameters for $R_0 < 1$.

Table 2. The sensitivity index of the suggested paradigm for $R_0 > 1$.

Parameters	Sensitivity index	Index values
ω	$\Theta_{\omega}^{R_0}$	66.0369
δ	$\Theta_{\delta}^{R_0}$	23.0415
τ	$\Theta_{\tau}^{R_0}$	-152.157
γ	$\Theta_{\gamma}^{R_0}$	-482.3430

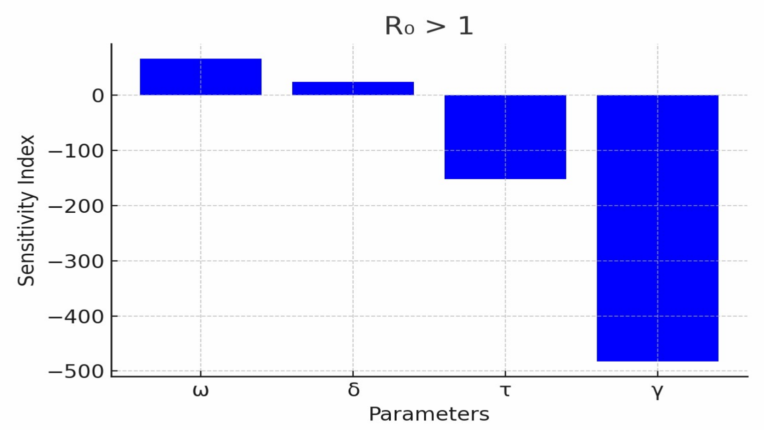

Figure 3. Sensitivity analysis of model parameters for $R_0 > 1$.

The sensitivity analysis, therefore, indicates that prevention is the most effective approach to treating illness.

3.3. Solution positivity

To ensure the well-posedness of the model (2.3), we verify the positivity and boundedness of its solutions.

Theorem 3.1. *For any $t > 0$, all solutions of* (2.3) *remain bounded and non-negative, provided that the initial conditions* (2.4) *are non-negative.*

Proof. To this end, we only need to consider any solution that starts in a non-negative direction. It is clear that

$$\begin{cases} {}^{FFM}\mathbb{D}_{0,t}^{\upsilon_1,\upsilon_2} S(t)\Big|_{S=0} = \omega \geq 0, \\ {}^{FFM}\mathbb{D}_{0,t}^{\upsilon_1,\upsilon_2} L(t)\Big|_{L=0} = 0 \geq 0, \\ {}^{FFM}\mathbb{D}_{0,t}^{\upsilon_1,\upsilon_2} R(t)\Big|_{R=0} = L\tau \geq 0. \end{cases}$$

The above confirms our theorem. □

3.4. Existence and uniqueness of the solutions

We begin by examining the existence and uniqueness of solutions to systems of equations in fractional calculus with a particular focus on applications in survival analysis. Furthermore, we assume that $\mathbf{U} = U(I) \times U(I) \times U(I)$ for the Banach space $U(I)$, which consists of real-valued continuous functions on the interval $I = [0, T]$, equipped with the norm

$$\|(S, L, R)\| \triangleq \|S\| + \|L\| + \|R\|,$$

where

$$\|S\| = \sup_{t\in I} |S(t)|, \ \|L\| = \sup_{t\in I} |L(t)||, \ \|R\| = \sup_{t\in I} |R(t)|.$$

By applying the FFM fractional integral operator defined in (2.2) to equations in (2.3), we obtain

$$\begin{cases} S(t) - S(0) &= {}^{FFM}\mathbb{I}_{0,t}^{\upsilon_1,\upsilon_2} \{\omega - \delta LS - \gamma S\}, \\ L(t) - L(0) &= {}^{FFM}\mathbb{I}_{0,t}^{\upsilon_1,\upsilon_2} \{\delta LS - (\gamma + \tau)L\}, \\ R(t) - R(0) &= {}^{FFM}\mathbb{I}_{0,t}^{\upsilon_1,\upsilon_2} \{L\tau - R\gamma\}. \end{cases} \tag{3.6}$$

To examine the existence and uniqueness of solutions for the system of equations in fractional survival analysis, we apply Definition 4.1 to (3.6), serving as the foundation for our analysis:

$$\begin{cases} S(t) - S(0) &= \dfrac{1-\upsilon_1}{H(\upsilon_1)} G_1(t, S(t)) + \dfrac{\upsilon_1}{H(\upsilon_1)\Gamma(\upsilon_1)} \displaystyle\int_0^t (t-s)^{\upsilon_1-1} G_1(s, S(s)) ds, \\ L(t) - L(0) &= \dfrac{1-\upsilon_1}{H(\upsilon_1)} G_2(t, L(t)) + \dfrac{\upsilon_1}{H(\upsilon_1)\Gamma(\upsilon_1)} \displaystyle\int_0^t (t-s)^{\upsilon_1-1} G_2(s, L(s)) ds, \\ R(t) - R(0) &= \dfrac{1-\upsilon_1}{H(\upsilon_1)} G_3(t, R(t)) + \dfrac{\upsilon_1}{H(\upsilon_1)\Gamma(\upsilon_1)} \displaystyle\int_0^t (t-s)^{\upsilon_1-1} G_3(s, R(s)) ds, \end{cases} \tag{3.7}$$

where

$$\begin{cases} G_1(t,S(t)) &=& \omega-\delta LS-\gamma S,\\ G_2(t,L(t)) &=& \delta LS-(\gamma+\tau)L,\\ G_3(t,R(t)) &=& L\tau-R\gamma. \end{cases} \tag{3.8}$$

Functions $G_1(t,S(t))$, $G_2(t,L(t))$, and $G_3(t,R(t))$ satisfy the Lipschitz condition if and only if $S(t)$, $L(t)$ and $R(t)$ are upper bounded. Given the assumption that $S(t)$ and $\tilde{S}(t)$ are continuous functions, the preceding analysis indicates that

$$\|G_1(t,S(t))-G_1(t,\tilde{S}(t))\| = \|\{\omega-(\delta L+\gamma)S\}-\{\omega-(\delta L+\gamma)\tilde{S}\}\| = \|-(\delta L+\gamma)(S-\tilde{S})\|.$$

Hence,

$$\|G_1(t,S(t))-G_1(t,\tilde{S}(t))\| \le \|\delta L+\gamma\|\cdot\|S-\tilde{S}\|.$$

$L\in U(I)$ is bounded, so we let $K_1=\|\delta L+\gamma\|$, which then leads to

$$\|G_1(t,S(t))-G_1(t,\tilde{S}(t))\| \le K_1\|S-\tilde{S}\|. \tag{3.9}$$

Similarly, we have

$$\begin{aligned} \|G_2(t,L(t))-G_2(t,\tilde{L}(t))\| &\le K_2\|L-\tilde{L}\|,\\ \|G_3(t,R(t))-G_3(t,\tilde{R}(t))\| &\le K_3\|R-\tilde{R}\|, \end{aligned} \tag{3.10}$$

where $K_2=\|\delta S+(\gamma+\tau)\|$ and $K_3=\gamma$. Since K_1, K_2, and K_3 are Lipschitz constants for functions G_1, G_2, and G_3, respectively, equations in (3.7) can be expressed recursively as

$$\begin{cases} S_n(t) &=& S(0)+\dfrac{1-\upsilon_1}{H(\upsilon_1)}G_1(t,S_{n-1}(t))+\dfrac{\upsilon_1}{H(\upsilon_1)\Gamma(\upsilon_1)}\displaystyle\int_0^t(t-s)^{\upsilon_1-1}G_1(s,S_{n-1}(s))ds,\\ L_n(t) &=& L(0)+\dfrac{1-\upsilon_1}{H(\upsilon_1)}G_2(t,L_{n-1}(t))+\dfrac{\upsilon_1}{H(\upsilon_1)\Gamma(\upsilon_1)}\displaystyle\int_0^t(t-s)^{\upsilon_1-1}G_2(s,L_{n-1}(s))ds,\\ R_n(t) &=& R(0)+\dfrac{1-\upsilon_1}{H(\upsilon_1)}G_3(t,R_{n-1}(t))+\dfrac{\upsilon_1}{H(\upsilon_1)\Gamma(\upsilon_1)}\displaystyle\int_0^t(t-s)^{\upsilon_1-1}G_3(s,R_{n-1}(s))ds. \end{cases} \tag{3.11}$$

Under the same initial conditions as those in (2.3), resolving the discrepancies yields the following:

$$\begin{cases} \Theta_{S,n}(t) &=& S_n(t)-S_{n-1}(t)=\dfrac{1-\upsilon_1}{H(\upsilon_1)}\left[G_1(t,S_{n-1}(t))-G_1(t,S_{n-2}(t))\right]\\ && +\dfrac{\upsilon_1}{H(\upsilon_1)\Gamma(\upsilon_1)}\displaystyle\int_0^t(t-s)^{\upsilon_1-1}\left[G_1(s,S_{n-1}(s))-G_1(s,S_{n-2}(s))\right]ds,\\ \Theta_{L,n}(t) &=& L_n(t)-L_{n-1}(t)=\dfrac{1-\upsilon_1}{H(\upsilon_1)}\left[G_2(t,L_{n-1}(t))-G_2(t,L_{n-2}(t))\right]\\ && +\dfrac{\upsilon_1}{H(\upsilon_1)\Gamma(\upsilon_1)}\displaystyle\int_0^t(t-s)^{\upsilon_1-1}\left[G_2(s,L_{n-1}(s))-G_2(s,L_{n-2}(s))\right]ds,\\ \Theta_{R,n}(t) &=& R_n(t)-R_{n-1}(t)=\dfrac{1-\upsilon_1}{H(\upsilon_1)}\{G_3(t,R_{-1+n}(t))-G_3(t,R_{n-2}(t))\}\\ && +\dfrac{\upsilon_1}{H(\upsilon_1)\Gamma(\upsilon_1)}\displaystyle\int_0^t(t-s)^{\upsilon_1-1}\left[G_3(s,R_{n-1}(s))-G_3(s,R_{n-2}(s))\right]ds. \end{cases} \tag{3.12}$$

Consequently,

$$S_n(t) = \sum_{p=1}^{n} \Theta_{S,p}(t), \ \ L_n(t) = \sum_{p=1}^{n} \Theta_{L,p}(t), \ \ R_n(t) = \sum_{p=1}^{n} \Theta_{R,p}(t). \tag{3.13}$$

By applying Eqs (3.9), (3.10), and (3.13), we derive the following set of inequalities:

$$\begin{cases} \|\Theta_{S,n}(t)\| \leq \dfrac{1-\upsilon_1}{H(\upsilon_1)} K_1 \|\Theta_{S,n-1}(t)\| + \dfrac{\upsilon_1}{H(\upsilon_1)\Gamma(\upsilon_1)} \displaystyle\int_0^t (t-s)^{\upsilon_1 - 1} K_1 \|\Theta_{S,n-1}(s)\| ds, \\ \|\Theta_{L,n}(t)\| \leq \dfrac{1-\upsilon_1}{H(\upsilon_1)} K_2 \|\Theta_{L,n-1}(t)\| + \dfrac{\upsilon_1}{H(\upsilon_1)\Gamma(\upsilon_1)} \displaystyle\int_0^t (t-s)^{\upsilon_1 - 1} K_2 \|\Theta_{L,n-1}(s)\| ds, \\ \|\Theta_{R,n}(t)\| \leq \dfrac{1-\upsilon_1}{H(\upsilon_1)} K_3 \|\Theta_{R,n-1}(t)\| + \dfrac{\upsilon_1}{H(\upsilon_1)\Gamma(\upsilon_1)} \displaystyle\int_0^t (t-s)^{\upsilon_1 - 1} K_3 \|\Theta_{R,n-1}(s)\| ds. \end{cases} \tag{3.14}$$

Theorem 3.2. *Assume that*

$$\Upsilon_i \equiv \left(\frac{1-\upsilon_1}{H(\upsilon_1)} + \frac{k^{\upsilon_1}}{H(\upsilon_1)\Gamma(\upsilon_1)} \right) K_i < 1, \ \ i = 1, 2, 3, \tag{3.15}$$

for a positive constant k. Then the solution to the proposed fractional-order FFM model of mumps disease transmission (2.3) *is unique for $t \in I$.*

Proof. Since the functions $S(t), L(t), R(t) \in U(I)$ are bounded, and the quantities G_1, G_2, and G_3 satisfy the Lipschitz condition, as shown in Eqs (3.9) and (3.10) by applying a recursive approach and using Eq (3.13), we obtain the following inequalities:

$$\begin{cases} \|\Theta_{S,n}(t)\| & \leq & \|S_0(t)\| \Upsilon_1^n, \\ \|\Theta_{L,n}(t)\| & \leq & \|L_0(t)\| \Upsilon_2^n, \\ \|\Theta_{R,n}(t)\| & \leq & \|R_0(t)\| \Upsilon_3^n. \end{cases} \tag{3.16}$$

As observed clearly, relations (3.16) have the property that $\|\Theta_{S,n}(t)\| \to 0$, $\|\Theta_{L,n}(t)\| \to 0$, and $\|\Theta_{R,n}(t)\| \to 0$ as $n \to \infty$. Moreover, by applying the triangle inequality to (3.16), we conclude that

$$\begin{cases} \|S_{n+j}(t) - S_n(t)\| & \leq & \displaystyle\sum_{i=n+1}^{n+j} \Upsilon_1^i = \dfrac{\Upsilon_1^{n+1} - \Upsilon_1^{n+j+1}}{1-\Upsilon_1}, \\ \|L_{n+j}(t) - L_n(t)\| & \leq & \displaystyle\sum_{i=n+1}^{n+j} \Upsilon_2^i = \dfrac{\Upsilon_2^{n+1} - \Upsilon_2^{n+j+1}}{1-\Upsilon_2}, \quad \text{for all } j \geq 1. \\ \|R_{n+j}(t) - R_n(t)\| & \leq & \displaystyle\sum_{i=n+1}^{n+j} \Upsilon_3^i = \dfrac{\Upsilon_3^{n+1} - \Upsilon_3^{n+j+1}}{1-\Upsilon_3}, \end{cases} \tag{3.17}$$

Here, the constraint (3.15) always remains valid. Consequently, $\left\{S_j(t)\right\}_{j=1}^{\infty}$, $\left\{L_j(t)\right\}_{j=1}^{\infty}$, and $\left\{R_j(t)\right\}_{j=1}^{\infty}$ are Cauchy sequences, and they therefore converge uniformly.

By letting n approach to ∞ in (3.11), it is clear that the limits of the resulting sequences converge to unique solutions for the framework described in Eq (2.3). Therefore, the uniqueness of solutions for the mumps virus transmission dynamics governed by the FFM fractional operator has been confirmed. □

4. Stability analysis

Ulam-Hyers (UH) stability analysis has been shown to reveal valuable characteristics for the simulation procedures used in epidemics [17]. As a result, this analysis has gained popularity among researchers simulating complex epidemic problems. In the following study, we will perform a UH-type stability analysis for the transmission dynamics calculated through the mumps virus model (2.3), particularly in response to slight variations in initial conditions. We will demonstrate that (2.3) is UH stable.

Definition 4.1. *The model (2.3) is UH stable if for* $\hbar_i > 0, \aleph_i > 0$*,* $i = 1,2,3$*, and for every* $(\tilde{S}, \tilde{L}, \tilde{R})$*,* $(S, L, R) \in \mathbf{U}$ *satisfy*

$$\begin{aligned} \|\tilde{S}(t) - G_1(t, S(t))\| &\leq \hbar_1, \\ \|\tilde{L}(t) - G_2(t, L(t))\| &\leq \hbar_2, \\ \|\tilde{R}(t) - G_3(t, R(t))\| &\leq \hbar_3. \end{aligned} \tag{4.1}$$

Then we have

$$\begin{aligned} \|\tilde{S}(t) - G_1(t, S(t))\| &\leq \hbar_1 \aleph_1(t), \\ \|\tilde{L}(t) - G_2(t, L(t))\| &\leq \hbar_2 \aleph_2(t), \\ \|\tilde{R}(t) - G_3(t, R(t))\| &\leq \hbar_3 \aleph_3(t). \end{aligned} \tag{4.2}$$

Remark 4.1. *Following [17], there exists an* $\aleph_i(t) \in U(I)$ *such that* $\|\aleph_i(t)\| < \hbar_i$*, for any* $t \in I$*. The components* $(\tilde{S}, \tilde{L}, \tilde{R})$ *satisfy the following relationships:*

$$\begin{aligned} \tilde{S}(t) &= G_1(t, S(t)) + \aleph_1(t), \\ \tilde{L}(t) &= G_2(t, L(t)) + \aleph_2(t), \\ \tilde{R}(t) &= G_3(t, R(t)) + \aleph_3(t). \end{aligned} \tag{4.3}$$

Lemma 4.1. *Assume that for every* $\hbar_i > 0$*,* $(\tilde{S}, \tilde{L}, \tilde{R}) \in \wp$ *is a solution to the system of inequalities (4.1). Then, the functions* $(S, L, R) \in \mathbf{U}$ *must satisfy the following inequalities*

$$\begin{aligned} &\|\tilde{S}(t) - \left(S(0) + \frac{G_1(t, S(t))(1-\upsilon_1)}{H(\upsilon_1)}\right) - \frac{\upsilon_1}{H(\upsilon_1 \Gamma(\upsilon_1))} \int_0^t (t-s)^{\upsilon_1 - 1} G_1(s, S(s)) ds\| \\ &\leq \left(\frac{(1-\upsilon_1)}{H(\Upsilon^{\upsilon_1})} + \frac{\upsilon_1}{H(\upsilon_1)\Gamma(\upsilon_1)}\right)\hbar_1, \\ &\|\tilde{L}(t) - \left(L(0) + \frac{G_2(t, L(t))(1-\upsilon_1)}{H(\upsilon_1)}\right) - \frac{\upsilon_1}{H(\upsilon_1 \Gamma(\upsilon_1))} \int_0^t (t-s)^{\upsilon_1 - 1} G_2(s, L(s)) ds\| \\ &\leq \left(\frac{(1-\upsilon_1)}{H(\Upsilon^{\upsilon_1})} + \frac{\upsilon_1}{H(\upsilon_1)\Gamma(\upsilon_1)}\right)\hbar_2, \\ &\|\tilde{R}(t) - \left(R(0) + \frac{G_3(t, R(t))(1-\upsilon_1)}{H(\upsilon_1)}\right) - \frac{\upsilon_1}{H(\upsilon_1 \Gamma(\upsilon_1))} \int_0^t (t-s)^{\upsilon_1 - 1} G_3(s, R(s)) ds\| \\ &\leq \left(\frac{(1-\upsilon_1)}{H(\Upsilon^{\upsilon_1})} + \frac{\upsilon_1}{H(\upsilon_1)\Gamma(\upsilon_1)}\right)\hbar_3. \end{aligned} \tag{4.4}$$

Proof. For a given $\tilde{S} \in U([0,T])$, let $\hbar_i > 0,\ i = 1,2,3$. Then, the following inequalities hold

$$\begin{aligned} \|\tilde{S}(t) - G_1(t,S(t))\| &\leq \hbar_1, \\ \|\tilde{L}(t) - G_2(t,L(t))\| &\leq \hbar_2, \\ \|\tilde{R}(t) - G_3(t,R(t))\| &\leq \hbar_3. \end{aligned}$$

Recall Remark 4.1, and it follows immediately that

$$\begin{aligned} \tilde{S}(t) &= G_1(t,S(t)) + N_1(t), \\ \tilde{L}(t) &= G_2(t,L(t)) + N_2(t), \\ \tilde{R}(t) &= G_3(t,R(t)) + N_3(t), \end{aligned}$$

where $\|N_1(t)\| \leq \hbar_1$, $\|N_2(t)\| \leq \hbar_2$, and $\|N_3(t)\| \leq \hbar_3$. Thus, we have

$$\begin{aligned} \tilde{S}(t) &= \tilde{S}(0) + \frac{(1-\upsilon_1)}{H(\upsilon_1)}\left[G_1(t,S(t)) - N_1(t)\right] + \frac{\upsilon_1}{H(\upsilon_1)\Gamma(\upsilon_1)}\int_0^t \left[G_1(s,S(s)) - N_1(s)\right] ds, \\ \tilde{L}(t) &= \tilde{L}(0) + \frac{(1-\upsilon_1)}{H(\upsilon_1)}\left[G_2(t,L(t)) - N_2(t)\right] + \frac{\upsilon_1}{H(\upsilon_1)\Gamma(\upsilon_1)}\int_0^t \left[G_2(s,L(s)) - N_2(s)\right] ds, \\ \tilde{R}(t) &= \tilde{R}(0) + \frac{(1-\upsilon_1)}{H(\upsilon_1)}\left[G_3(t,R(t)) - N_3(t)\right] + \frac{\upsilon_1}{H(\upsilon_1)\Gamma(\upsilon_1)}\int_0^t \left[G_3(s,R(s)) - N_3(s)\right] ds. \end{aligned}$$

Consequently, we acquire that

$$\begin{aligned} &\left\|\tilde{S}(t) - \left(S(0) + \frac{(1-\upsilon_1)G_1(t,S(t))}{H(\upsilon_1)}\right) + \frac{\upsilon_1}{H(\upsilon_1)\Gamma(\upsilon_1)}\int_0^t (t-s)^{\upsilon_1-1} G_1(s,S(s))ds\right\| \\ \leq\ & \frac{(1-\upsilon_1)\|N_1(t)\|}{H(\upsilon_1)} + \frac{\upsilon_1}{H(\upsilon_1)\Gamma(\upsilon_1)}\int_0^t (t-s)^{\upsilon_1-1}|N_1(s)|ds \leq \left(\frac{(1-\upsilon_1)}{H(\Upsilon^{\upsilon_1})} + \frac{\upsilon_1}{H(\upsilon_1)\Gamma(\upsilon_1)}\right)\hbar_1, \\ &\left\|\tilde{L}(t) - \left(L(0) + \frac{(1-\upsilon_1)G_2(t,L(t))}{H(\upsilon_1)}\right) + \frac{\upsilon_1}{H(\upsilon_1)\Gamma(\upsilon_1)}\int_0^t (t-s)^{\upsilon_1-1} G_2(s,L(s))ds\right\| \\ \leq\ & \frac{(1-\upsilon_1)\|N_2(t)\|}{H(\upsilon_1)} + \frac{\upsilon_1}{H(\upsilon_1)\Gamma(\upsilon_1)}\int_0^t (t-s)^{\upsilon_1-1}|N_2(s)|ds \leq \left(\frac{(1-\upsilon_1)}{H(\Upsilon^{\upsilon_1})} + \frac{\upsilon_1}{H(\upsilon_1)\Gamma(\upsilon_1)}\right)\hbar_2, \\ &\left\|\tilde{R}(t) - \left(R(0) + \frac{(1-\upsilon_1)G_3(t,R(t))}{H(\upsilon_1)}\right) + \frac{\upsilon_1}{H(\upsilon_1)\Gamma(\upsilon_1)}\int_0^t (t-s)^{\upsilon_1-1} G_3(s,R(s))ds\right\| \\ \leq\ & \frac{(1-\upsilon_1)\|N_3(t)\|}{H(\upsilon_1)} + \frac{\upsilon_1}{H(\upsilon_1)\Gamma(\upsilon_1)}\int_0^t (t-s)^{\upsilon_1-1}|N_3(s)|ds \leq \left(\frac{(1-\upsilon_1)}{H(\Upsilon^{\upsilon_1})} + \frac{\upsilon_1}{H(\upsilon_1)\Gamma(\upsilon_1)}\right)\hbar_3. \end{aligned}$$

Thus, inequalities in (4.4) are confirmed. Other inequalities can be proved similarly. □

Theorem 4.1. *Suppose that conditions (3.9) and (3.10) are satisfied. Then, the fractional model (2.3) is HU stable, provided that the following inequality holds*

$$\left(\frac{1-\upsilon_1}{H(\upsilon_1)} + \frac{\Upsilon^{\upsilon_1}}{H(\upsilon_1)\Gamma(\upsilon_1)}\right)K_i < 1,$$

where $K_i > 0$, $i = 1, 2, 3$, *are the Lipschitz constants.*

Proof. Since $\tilde{S} \in U(I)$ holds for (4.1), we let $\hbar_1 > 0$. Additionally, assume that $S(t) \in U(I)$ is the unique solution to the proposed fractional model (2.3). We have

$$S(t) = S(0) + \frac{(1-\upsilon_1)H(t, S(t))}{H(\upsilon_1)} + \frac{\upsilon_1}{H(\upsilon_1)\Gamma(\upsilon_1)} \int_0^t (t-s)^{\upsilon_1 - 1} H_1(s, S(s))\, ds. \tag{4.5}$$

By applying the properties of the triangle inequality and Lemma 4.1, we find that

$$\begin{aligned} \left\|\tilde{S}(t) - S(t)\right\| \leq & \left\|\tilde{S}(0) - \Big(S(0) + \frac{(1-\upsilon_1)H(t, S(t))}{H(\upsilon_1)} + \frac{\upsilon_1}{H(\upsilon_1)\Gamma(\upsilon_1)} \int_0^t (t-s)^{\upsilon_1 - 1} H(s, S(s))\, ds\Big)\right\| \\ & + \frac{(1-\upsilon_1)}{H(\upsilon_1)} \left\|H(t, S(t)) - H(t, \tilde{S}(t))\right\| + \frac{\upsilon_1}{H(\upsilon_1)\Gamma(\upsilon_1)} \int_0^t \left\|H(s, S(s)) - H(k, \tilde{S}(t))\right\| ds \\ \leq & \left[\frac{(1-\upsilon_1)}{H(\upsilon_1)} + \frac{\Upsilon^{\upsilon_1}}{H(\upsilon_1)\Gamma(\upsilon_1)}\right] K_1^d \|\tilde{S}(t) - S(t)\|. \end{aligned}$$

Following Lemma 4.1, we have

$$\|\tilde{S}(t) - S(t)\| \leq \frac{\left[\frac{(1-\upsilon_1)}{H(\upsilon_1)} + \frac{\Upsilon^{\upsilon_1}}{H(\upsilon_1)\Gamma(\upsilon_1)}\right]\hbar_1}{1 - \left[\frac{(1-\upsilon_1)}{H(\upsilon_1)} + \frac{\Upsilon^{\upsilon_1}}{H(\upsilon_1)\Gamma(\upsilon_1)}\right] K_1^d} = \Upsilon_1 \hbar_1,$$

where

$$\Upsilon_1 = \frac{\left[\frac{(1-\upsilon_1)}{H(\upsilon_1)} + \frac{\Upsilon^{\upsilon_1}}{H(\upsilon_1)\Gamma(\upsilon_1)}\right]}{1 - \left[\frac{(1-\upsilon_1)}{H(\upsilon_1)} + \frac{\Upsilon^{\upsilon_1}}{H(\upsilon_1)\Gamma(\upsilon_1)}\right] K_1^d}.$$

Similarly, we may obtain

$$\|\tilde{L}(t) - L(t)\| \leq \Upsilon_2 \hbar_2, \quad \|\tilde{R}(t) - R(t)\| \leq \Upsilon_3 \hbar_3.$$

Thus, the proposed FFM model (2.3) is HU-stable. □

5. Simulation frameworks

We are particularly interested in a case problem proposed in [15]. The initial value problem is given by

$$\begin{cases} {}^{FFM}\mathbb{D}_{0,t}^{\upsilon_1, \upsilon_2} \psi(t) = \Upsilon(t, \psi(t)), \\ \psi(0) = \psi_0. \end{cases} \tag{5.1}$$

We reformulate the above using the newly established fractional integral with the Mittag-Leffler kernel to

$$\psi(t) = \psi(0) + \frac{1-\upsilon_1}{H(\upsilon_1)} t^{1-\upsilon_2} \Upsilon(t, \psi(t)) + \frac{\upsilon_1}{H(\upsilon_1)\Gamma(\upsilon_1)} \int_0^t (t-\mu)^{\upsilon_1 - 1} \Upsilon(\mu, \psi(\mu)) \mu^{1-\upsilon_2}\, d\mu.$$

Assume the partition grid is uniform with $t_i = i\Delta t, i = 0, 1, \cdots, n$. The solution at $t = t_{n+1}$ is expressed as:

$$\psi(t_{n+1}) \;=\; \psi(0) \;+\; \frac{1-\upsilon_1}{H(\upsilon_1)} t_n^{1-\upsilon_2}\Upsilon(t_n,\psi(t_{n+1})) \;+\; \frac{\upsilon_1}{H(\upsilon_1)\Gamma(\upsilon_1)}\int_0^{t_{n+1}}(t_{n+1} \;-\; \mu)^{\upsilon_1-1}\Upsilon(\mu,\psi(\mu))\mu^{1-\upsilon_2}\,d\mu.$$

For simplicity, we define the following

$$\Psi(t,\psi(t)) = \Upsilon(t,\psi(t))t^{1-\upsilon_2}. \tag{5.2}$$

In addition, we have

$$\psi(t_{n+1}) = \psi(0) + \frac{1-\upsilon_1}{H(\upsilon_1)}\Psi(t_{n+1},\psi(t_{n+1})) + \frac{\upsilon_1}{H(\upsilon_1)\Gamma(\upsilon_1)}\sum_{i=2}^{n}\int_{t_i}^{t_{i+1}}\Psi(\mu,\psi(\mu))(t_{n+1}-\mu)^{\upsilon_1-1}d\mu.$$

Since the above function is in implicit form, we use an approximate technique as in [15]. One uses Newton polynomial for the approximation ψ_{n+1} to approach $\psi(t_{n+1})$ and by letting the known values $\psi_i = \psi(t_i)$ for all $i, 0 \leq i \leq n$. This substitution enables the equation to be rewritten into a form suitable for further analysis and calculations. This leads to

$$\begin{aligned}\psi_{n+1} =&\psi(0) + \frac{1-\upsilon_1}{H(\upsilon_1)}\Psi(t_{n+1},\psi_{n+1}) + \frac{\upsilon_1}{H(\upsilon_1)\Gamma(\upsilon_1)}\Bigg[\;\sum_{i=2}^{n}\Psi(t_{i-2},\psi_{i-2})\Delta t\int_{t_i}^{t_{i+1}}(t_{n+1}-\mu)^{\upsilon_1-1}d\mu\\ &+\sum_{i=2}^{n}\frac{\Psi(t_{i-1},\psi_{i-1})-\Psi(t_{i-2},\psi_{i-2})}{\Delta t}\int_{t_i}^{t_{i+1}}(\mu-t_{i-2})(t_{n+1}-\mu)^{\upsilon_1-1}d\mu\\ &+\sum_{i=2}^{n}\frac{\Psi(t_i,\psi_i)-2\Psi(t_{i-1},\psi_{i-1})+\Psi(t_{i-2},\psi_{i-2})}{2(\Delta t)^2}\int_{t_i}^{t_{i+1}}(\mu-t_{i-2})(\mu-t_{i-1})(t_{n+1}-\mu)^{\upsilon_1-1}d\mu\Bigg].\end{aligned} \tag{5.3}$$

Integrals in (5.3) can be evaluated as follows:

$$\int_{t_i}^{t_{i+1}}(t_{n+1}-\mu)^{\upsilon_1-1}d\mu = \frac{(\Delta t)^{\upsilon_1}}{\upsilon_1}\left[(n-i+1)^{\upsilon_1}-(n-i)^{\upsilon_1}\right],$$

$$\int_{t_i}^{t_{i+1}}(\mu-t_{i-2})(t_{n+1}-\mu)^{\upsilon_1-1}d\mu = \frac{(\Delta t)^{\upsilon_1+1}}{\upsilon_1(\upsilon_1+1)}\times\Big[(n-i)^{\upsilon_1}(2\upsilon_1+1-i+n)-(n-i)^{\upsilon_1}(3\upsilon_1-i+n-1)\Big],$$

and

$$\begin{aligned}&\int_{t_i}^{t_{i+1}}(\mu-t_{i-2})(\mu-t_{i-1})(t_{n+1}-\mu)^{\upsilon_1-1}d\mu\\ &=\frac{(\Delta t)^{\upsilon_1+2}}{\upsilon_1(\upsilon_1+1)(\upsilon_1+2)}\times\Big[(n+1-i)^{\upsilon_1}\{2(n-i)^2+(n-i)(3\upsilon_1+10)+2\upsilon_1^2+9\upsilon_1+12\}\\ &\quad-(n-i)^{\upsilon_1}\{2(n-i)^2+(5\upsilon_1+10)(n-i)+18\upsilon_1+6\upsilon_1^2+12\}\Big].\end{aligned}$$

Substituting the above in (5.3) with the initial guess $\psi_{n+1}^{(0)} = \psi_n$ and incorporating the initial value problem (5.1), we obtain the following numerical scheme: for $k = 1, 2, \cdots$,

$$\begin{aligned}\psi_{n+1}^{(k)} &= \psi(0) + \frac{1-\upsilon_1}{H(\upsilon_1)}\Upsilon(t_{n+1}, \psi_{n+1}^{(k-1)})t_{n+1}^{1-\upsilon_2} + \frac{\upsilon_1(\Delta t)^{\upsilon_1}}{H(\upsilon_1)\Gamma(\upsilon_1+1)}\Bigg\{\sum_{i=2}^{n}\Upsilon(t_{i-2}, \psi_{i-2})t_{i-2}^{1-\upsilon_2}\\
&\times[(n-i)^{\upsilon_1} - (n-i+1)^{\upsilon_1}] + \sum_{i=2}^{n}\Big[\Upsilon(t_{i-1}, \psi_{i-1})t_{i-1}^{1-\upsilon_2} - \Upsilon(t_{i-2}, \psi_{i-2})t_{i-2}^{1-\upsilon_2}\Big]\\
&\times[(n-i+1)^{\upsilon_1}(2\upsilon_1 + n - i + 3) - (n-i)^{\upsilon_1}(3\upsilon_1 + 3 + n - i)]\\
&+ \sum_{i=2}^{n}\Big[\Upsilon(t_i, \psi_i)t_i^{1-\upsilon_2} - 2\Upsilon(t_{i-1}, \psi_{i-1})t_{i-1}^{1-\upsilon_2} + \Upsilon(t_{i-2}, \psi_{i-2})t_{i-2}^{1-\upsilon_2}\Big]\\
&\times\Big[(n-i+1)^{\upsilon_1}\Big(2(n-i)^2 + (3\upsilon_1+10)(n-i) + 2\upsilon_1^2 + 9\upsilon_1 + 12\Big)\\
&-(n-i)^{\upsilon_1}\Big(2(n-i)^2 + (5\upsilon_1+10)(n-i) + 6\upsilon_1^2 + 18\upsilon_1 + 12\Big)\Big]\Bigg\}.\end{aligned}$$

The above equations can be expressed recursively, and this generates a sequence of series $\left\{\psi_{n+1}^{(k)}\right\}_{k=0}^{\infty}$ for $\psi(t_{n+1})$. This algorithm is used for evaluating the values of $S(t)$, $L(t)$, $T(t)$, for all $t > 0$.

6. Numerical simulations and discussions

This section conducts advanced numerical simulations of nonlinear mumps virus models with therapeutic interventions, highlighting the influence of fractional derivatives on treatment compartments. The fractal fractional derivative provides numerical solutions of various orders that align with the system's steady-state equilibrium. Additionally, these derivatives give generalized descriptions of memory effects and anomalous diffusion, which are often overlooked in classical models. Advanced numerical techniques further examine the dynamic behavior in response to parameter changes, offering insights into sensitivity related to fractional orders.

The new method underscores the complex relationship between therapeutic measures and the nonlinear dynamics of the mumps virus, highlighting the importance of epidemiological studies using fractional modeling. Figures 4–6 display estimated solutions for fractional orders where $R_0 < 1$. These figures demonstrate that as fractional values increase, $L(t)$ decreases, while $S(t)$ and $R(t)$ rise as fractional values decrease. All figures suggest that lowering fractional values leads to a steady state, indicating optimal performance when fractional values are below the classical derivative. These simulations show how variations in fractional orders impact the model's behavior, offering insights into the progression of mumps virus infection and enhancing the study's relevance for decision-making and control strategies.

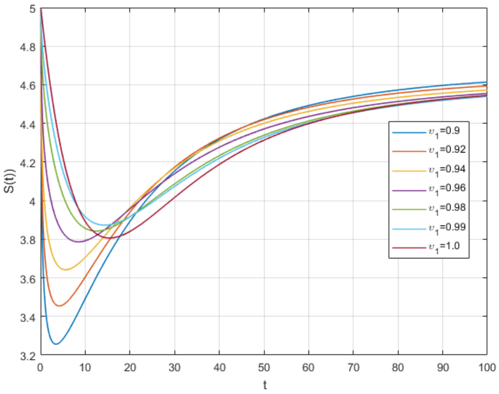

Figure 4. Simulation of the susceptible population $S(t)$ for various fractional-order values under the condition $R_0 < 1$.

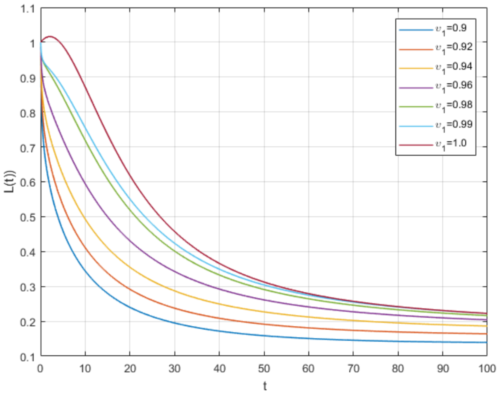

Figure 5. Simulation of the infected population $L(t)$ for various fractional-order values under the condition $R_0 < 1$.

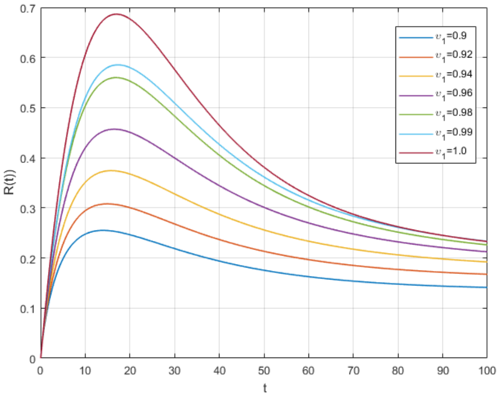

Figure 6. Simulation of the recovered population $R(t)$ for various fractional-order values under the condition $R_0 < 1$.

Figures 7–9 show the estimated solutions for different fractional orders when $R_0 > 1$. These figures demonstrate that $S(t)$ and $R(t)$ decrease as fractional values get lower, while $L(t)$ increases with higher fractional values. As the fractional values decrease, the behavior approaches a steady state, indicating that the model performs optimally when fractional values are lower than those of classical derivatives. These simulations highlight how altering the fractional order impacts the model's dynamics. They also demonstrate how the condition of individuals infected with the mumps virus evolves, underscoring the importance of this study in guiding decision-making and designing effective control strategies.

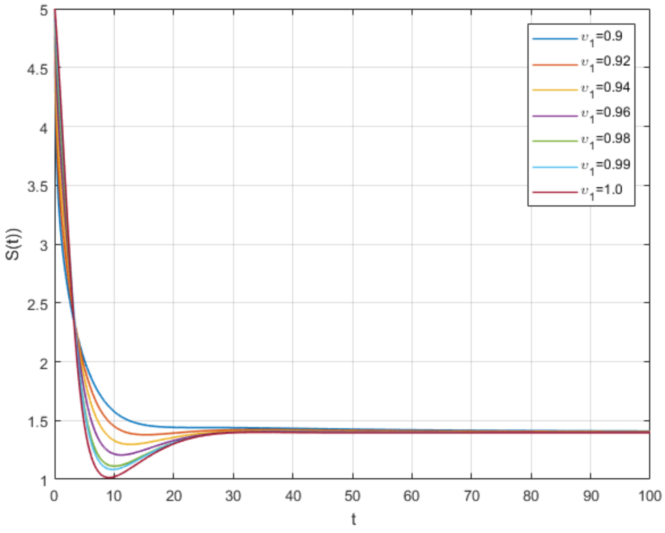

Figure 7. Simulation of the susceptible population $S(t)$ for various fractional-order values under the condition $R_0 > 1$.

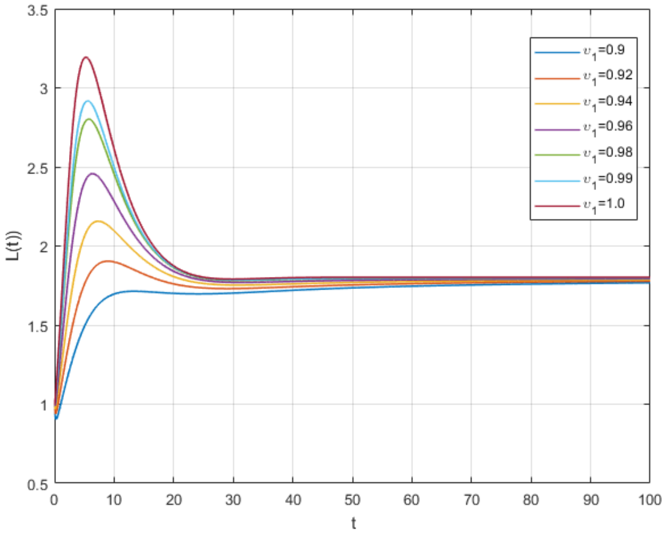

Figure 8. Simulation of the infected population $L(t)$ for various fractional-order values under the condition $R_0 > 1$.

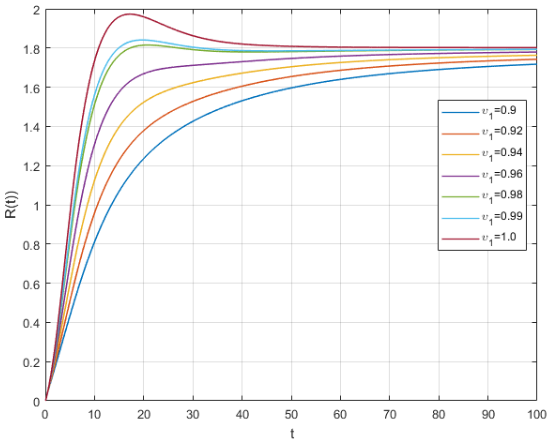

Figure 9. Simulation of the recovered population $R(t)$ for various fractional-order values under the condition $R_0 > 1$.

The computer simulations in the previous sections highlight the crucial impact of the mumps virus transmission rate on the reproduction number. When the transmission rate is $\delta = 0.0433$, the reproduction number reaches $R_0 = 0.99769585 < 1$, as shown in Figure 10, indicating that the virus is no longer spreading. Conversely, as seen in Figure 11, increasing the transmission rate to $\delta = 0.1433$ raises the reproduction number to $R_0 = 3.30184331797 > 1$, signaling ongoing disease transmission. These results suggest that isolating infected individuals and decreasing their interactions with susceptible individuals are very effective strategies for controlling mumps outbreaks during an epidemic.

This study employs Mittag-Leffler-type fractional derivatives, which capture the system's memory effects. The simulation results demonstrate that even small variations in the fractional derivative order can greatly influence the numerical outcomes. Therefore, determining the precise fractional order is crucial for obtaining accurate and dependable modeling results when real-world data is available.

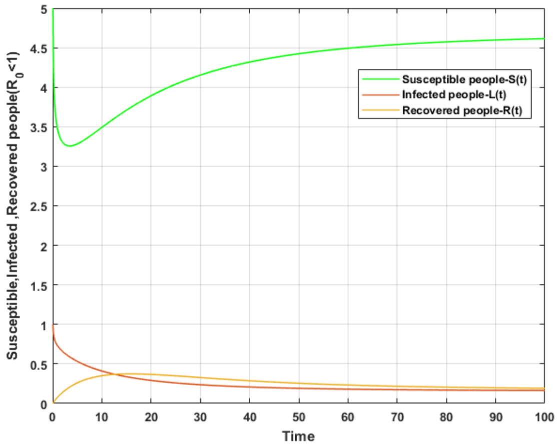

Figure 10. Numerical solutions for the susceptible population $S(t)$, the infected population $L(t)$, and the recovered population $R(t)$ under the condition $R_0 < 1$.

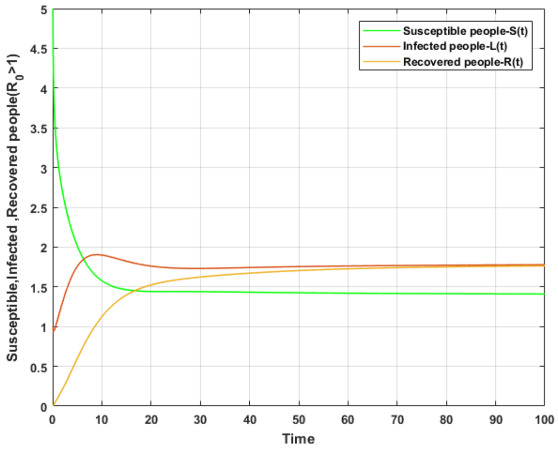

Figure 11. Numerical solutions for the susceptible population $S(t)$, the infected population $L(t)$, and the recovered population $R(t)$ under the condition $R_0 > 1$.

7. Artificial neural networks (ANNs)

ANNs offer a powerful tool in bioinformatics for modeling complex biological systems that are influenced by fractional calculus and high-dimensional data. Their flexibility makes them suitable for advanced biomathematical simulations, including applications in fractional disease modeling. ANNs identify patterns in fractional models based on biomathematical data, helping researchers understand and predict biological processes, especially in epidemiology. ANN is an effective data-processing method inspired by biological nervous systems, such as the human brain, which handle complex information through parallel computational models that imitate brain cell functions. Additionally, the extensive study of AI applications across various fields has been conducted, as detailed in references [18–20].

An ANN consists of many interconnected processing nodes called "neurons", linked by weighted connections. Each neuron receives input signals, processes them, and produces an output signal. The network includes weighted connections, an activation function that controls the neuron's output, and an aggregation function that combines input data based on connection strengths. The mathematical representation of the ANN process with N neurons in a single hidden layer is expressed as follows:

$$\begin{bmatrix} S \\ L \\ R \end{bmatrix} = \sigma\left(\begin{bmatrix} w_{11} & w_{12} & \cdots & w_{1N} \\ w_{21} & w_{22} & \cdots & w_{2N} \\ w_{31} & w_{32} & \cdots & w_{3N} \end{bmatrix} \begin{bmatrix} L_1 \\ L_2 \\ \vdots \\ L_N \end{bmatrix} + \begin{bmatrix} B_1 \\ B_2 \\ B_3 \end{bmatrix} \right), \tag{7.1}$$

where

- $\sigma(\cdot)$ represents the activation function (e.g., sigmoid, tanh, or ReLU),
- w_{ij} are the connection weights from hidden neurons to output neurons,
- B_j are the output bias terms,

- L_j are the latent variables from the hidden layer.

See [21, P. 168–203] for a detailed explanation of the architecture of deep feedforward networks.

Various methodologies apply ANNs to solve fractional differential equations in disease models, forming foundational steps for these applications. We present an ANN for solving fractional differential equations as follows:

- Parameters and variables: Begin by identifying the known parameters and the variables to be predicted or solved in the model.
- Data set: Develop a data set consisting of input-output pairs. The inputs should include relevant parameters and variables from the epidemiological model, while the outputs represent the expected results.
- Splitting data: Divide the data set into three groups: Training set, testing set, and validation set for deep learning.
- Optimize ANN: Minimize discrepancies between actual and predicted outputs by iteratively adjusting the weights and biases using a gradient descent optimizer or similar optimization methods.
- Evaluate model performance: Use statistical metrics such as Mean Squared Error (MSE), Root Mean Squared Error (RMSE), Mean Absolute Error (MAE), Coefficient of Determination (R^2), and Nash-Sutcliffe Efficiency (NSE) to assess the model's accuracy. Adjust the ANN structure or training parameters if performance is suboptimal.
- Validate predictions: Test the generalization ability of the ANN with new, untested data. Compare the ANN's predictions with known solutions or experimental results to ensure accuracy and reliability.
- Refine the model: If the model is inaccurate or new data becomes available, iteratively refine the ANN by revisiting some steps to enhance its accuracy and adaptability.

Effective data optimization is crucial for designing an ANN architecture that achieves outstanding performance. In our framework, datasets are divided into three sets: training (70%), testing (15%), and validation (15%). Our training set allows the model to learn effectively, while the validation set acts as a checkpoint for hyperparameter tuning and preventing overfitting. Lastly, the testing set, which the model has not encountered during training, objectively evaluates the model's predictive accuracy.

The ANN framework utilized in our procedure is well-designed to tackle complex biomathematical epidemiology models. These models often involve nonlinear mappings and complex dynamics, making them challenging to manage with conventional methods. To address such complexities, the ANN model employs a sigmoid activation function that transforms input values to a range between 0 and 1. This function is efficient for simulating probabilities or binary outcomes. As illustrated in Figure 12, the sigmoid activation function ensures that input values remain within the [0, 1] range, consistent with the model structure (2.3), and alleviating gradient-related issues.

The ANN architecture incorporates several critical design elements, including specific activation functions tailored to each layer described as

- Hidden layers: The Tan-Sigmoid activation function maps values between -1 and 1, providing the network with a broader dynamic range. This aids in learning both negative and positive correlations, enhancing the model's ability to detect patterns within the dataset.

- Output layer: A purlin activation function is utilized. This provides a straightforward linear transformation suitable for tasks that require real-valued outputs, such as regression or predicting continuous variables.

Further refinements of the fractional FFM model involve transfer function configurations incorporating a transfer mean activation, adjusting activation values relative to their average. This modification enables the model to capture subtle features in the data, thereby enhancing its adaptability and effectiveness across the training, validation, and testing phases, ensuring reliable and consistent performance.

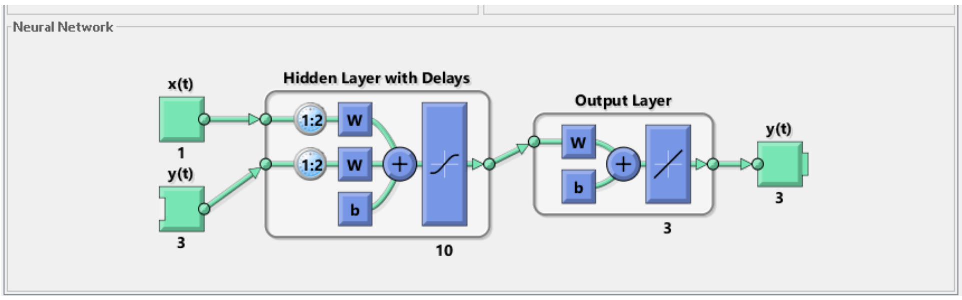

Figure 12. Architecture of the artificial neural network (ANN).

The sigmoid transfer function provides a powerful tool for nonlinear mapping, essential in time-series models used in epidemiology and biostatistics. It models stochastic growth patterns, offering insights into dynamic biological systems. By adding nonlinearity, the sigmoid function improves the model's ability to capture complex real-world interactions, making it vital for analyzing disease spread and population behaviors. Evaluations demonstrate the usefulness of our ANN in tackling real-world problems and advancing computational intelligence for public health and infectious disease research. Using these metrics helps researchers optimize ANN performance for studying disease patterns, boosting its role in public health initiatives. These metrics serve as guiding benchmarks for optimization, ensuring the model reaches the desired accuracy and effectiveness with real-world data.

8. Results and discussion

We aim to provide a comprehensive demonstration of complex self-regressive exogenous networks (ANNs) applied to the mumps viral model (2.3). Using the Mittag-Leffler kernel, the two-step Newtonian solver produces reference numerical results for two distinct scenarios, each involving six cases. The results, detailed in Tables 3–6 and Figures 13–29, highlight the effectiveness, reliability, and efficiency of our ANN method in managing sequential inputs and producing accurate predictions. The selection of sampling data for training and testing is crucial for maintaining the stability of the data distribution. Here, the datasets are divided into three sets: training (70%), testing (15%), and validation (15%), and we choose $k = 5$ in the k-fold cross-validation.

Figure 13 illustrates the reliability, consistency, and convergence of the aforementioned mumps model during the neural network's training phase. In Scenario 1 ($R_0 < 1$), the efficiency plot shows gradients of 9.95×10^{-8}, 9.98×10^{-8}, and 9.94×10^{-8} for $S(t)$, $L(t)$, and $R(t)$, respectively, at 220, 247, and 276 epochs. At these points, the cross-entropy error approaches zero. Similarly, in Scenario 2

($R_0 > 1$), as illustrated in Figure 14, the efficiency plot displays gradients of 9.92×10^{-8}, 9.79×10^{-8}, and 9.99×10^{-8} for $S(t)$, $L(t)$, and $R(t)$, respectively, at 458, 335, and 909 epochs, with the cross-entropy error once again approaching zero.

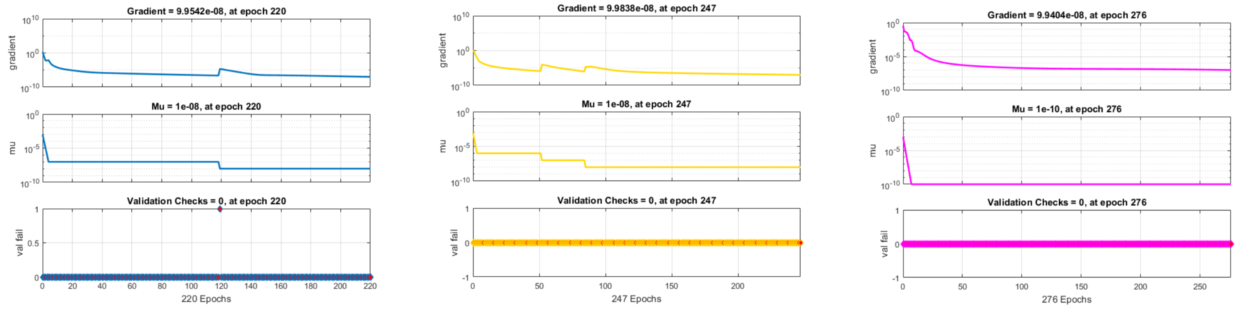

(a) $S(t)$ (b) $L(t)$ (c) $R(t)$

Figure 13. Adjustable monitoring parameters for the epidemiological analysis of the mumps model across all three classes in Scenario 1 ($R_0 < 1$).

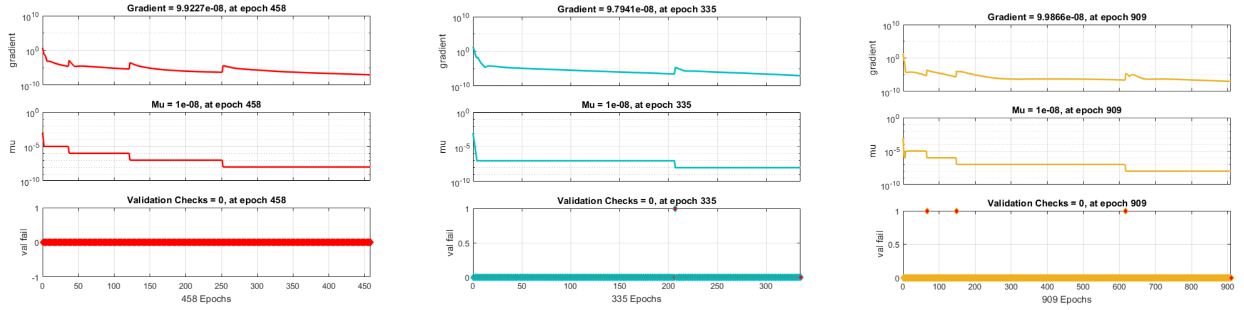

(a) $S(t)$ (b) $L(t)$ (c) $R(t)$

Figure 14. Adjustable monitoring parameters for the epidemiological analysis of the mumps model across all three classes in Scenario 2 ($R_0 > 1$).

The ANN framework effectively addresses the mumps viral model with minimal variation in key parameters. As the model reduces MSE during training, it enhances prediction accuracy, demonstrating reliability for complex epidemiological tasks. Figure 15 shows the converging learning curves of our ANNs for the proposed mumps viral model (2.3). In scenario 1 ($R_0 < 1$), MSE decreases for all classes, $S(t)$, $L(t)$, and $R(t)$, indicating improved accuracy as forecasts align more closely with actual data. MSE values for Scenario 1 are approximately 6.96E-11, 8.99E-11, and 1.06E-11 for $S(t)$, $L(t)$, and $R(t)$ at 220, 247, and 276 epochs, respectively.

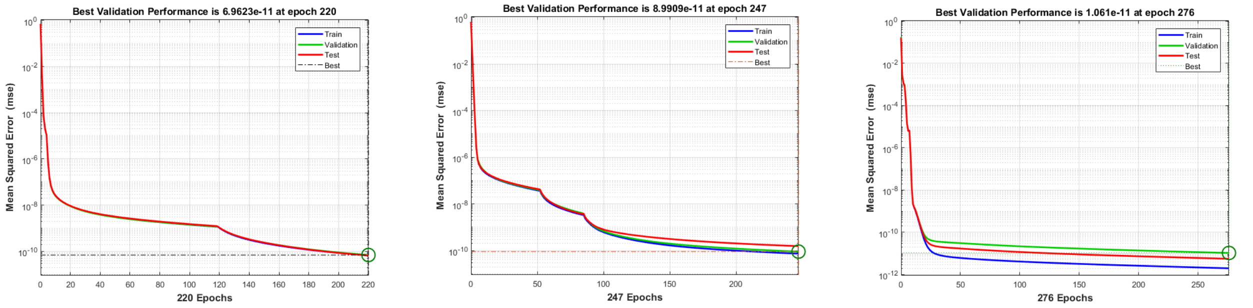

(a) $S(t)$ (b) $L(t)$ (c) $R(t)$

Figure 15. Learning curve plots showing the mean squared error (MSE) during training of the mumps epidemiological model for all three classes under Scenario 1 ($R_0 < 1$).

Similarly, Figure 16 shows converging curves for Scenario 2 ($R_0 > 1$). MSE values for the three classes in this scenario were approximately 2.41E-10, 1.13E-10, and 3.21E-11 at 458, 335, and 909 epochs, respectively. These MSE graphs highlight the importance of advanced computational methods in model optimization. Lower MSE indicates the model's better ability to capture underlying data patterns, demonstrating the effectiveness of the computational intelligence approach used.

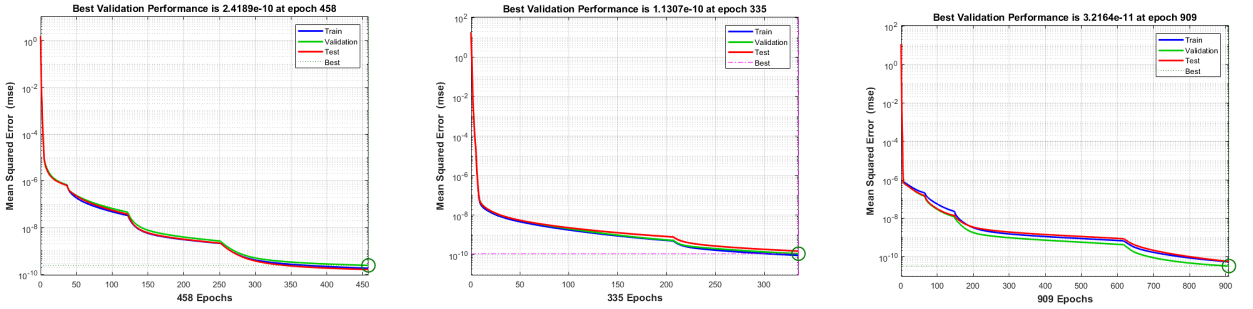

(a) $S(t)$ (b) $L(t)$ (c) $R(t)$

Figure 16. Learning curve plots showing the mean squared error (MSE) during training of the mumps epidemiological model for all three classes under Scenario 2 ($R_0 > 1$).

The serial correlation graphs for our ANN approach applied to the mumps viral model in both Scenario 1 ($R_0 < 1$) and Scenario 2 ($R_0 > 1$) across all three classes $S(t)$, $L(t)$, and $R(t)$, are shown in Figures 17 and 18, respectively. These graphs illustrate the gradual increase in connections between forecasting errors over time. The correlation ratios for all models, except at zero latency, fall within a 95% confidence interval, confirming the model's applicability and reliability.

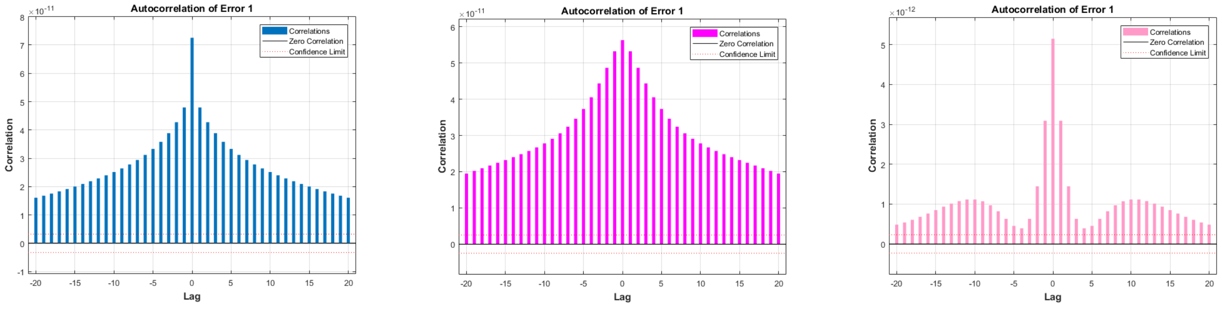

(a) $S(t)$ (b) $L(t)$ (c) $R(t)$

Figure 17. Serial correlation plots for the three epidemiological classes under Scenario 1 ($R_0 < 1$).

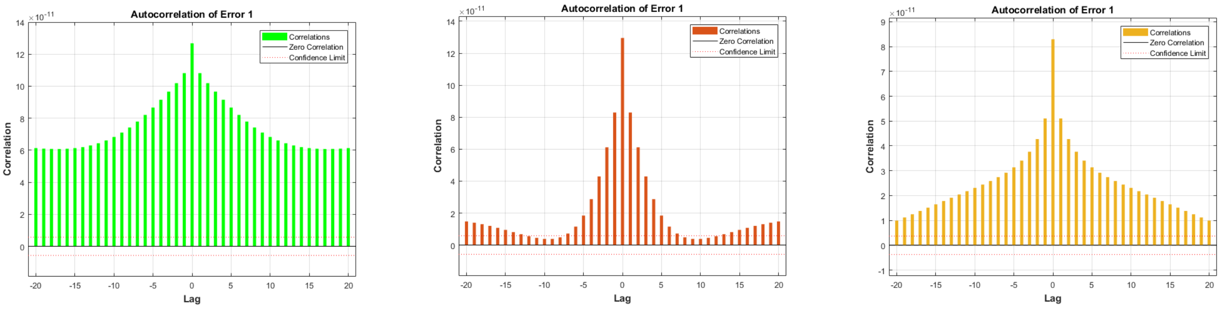

(a) $S(t)$ (b) $L(t)$ (c) $R(t)$

Figure 18. Serial correlation plots for the three epidemiological classes under Scenario 2 ($R_0 > 1$).

Additional validation of the system's network efficiency is shown in Figure 19 for Scenario 1 ($R_0 < 1$) and Figure 20 for Scenario 2 ($R_0 > 1$), highlighting the enhanced network efficacy across all three classes: $S(t)$, $L(t)$, and $R(t)$. The error values are depicted through error histogram plots. Specifically, Figure 21 illustrates the error histogram for the mumps viral model in Scenario 1 ($R_0 < 1$), while Figure 22 displays the error histogram for Scenario 2 ($R_0 > 1$). In these histograms, the vertical axis represents the frequency of error occurrences, while the horizontal axis indicates the error values at each instance. Our study utilizes a 20-bin error histogram to demonstrate that the proposed system achieves nearly 0% error. The histograms demonstrate the accuracy of the ANN computational technique, indicating that almost all error occurrences are concentrated in bars near the zero-error line. For $R_0 < 1$, the error magnitudes for $S(t)$, $L(t)$, and $R(t)$ are approximately -8.9E-06, -7E-06, and 4.19E-06, respectively. Likewise, for $R_0 > 1$, nearly all error occurrences for $S(t)$, $L(t)$, and $R(t)$ are located near the zero-error line, with error magnitudes of approximately -1.7E-06, -5.5E-06, and 2.05E-06, respectively. Error histograms are used to evaluate the effectiveness of the proposed ANN method in modeling mumps viral dynamics.

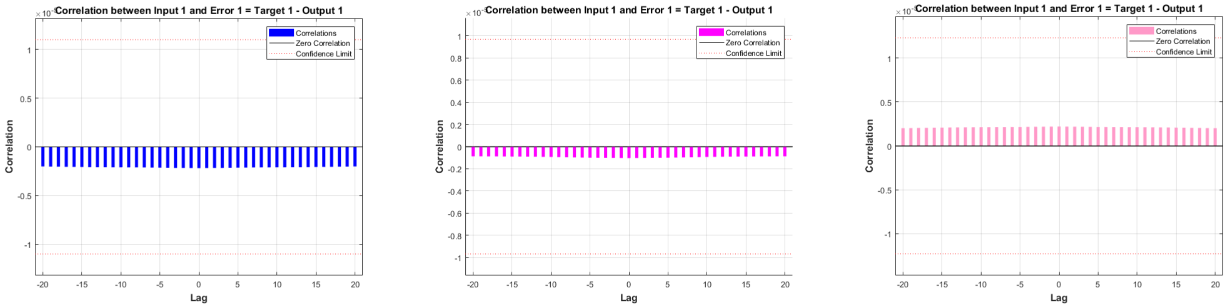

(a) $S(t)$ (b) $L(t)$ (c) $R(t)$

Figure 19. Input error correlation plots for all three epidemiological classes under Scenario 1 ($R_0 < 1$).

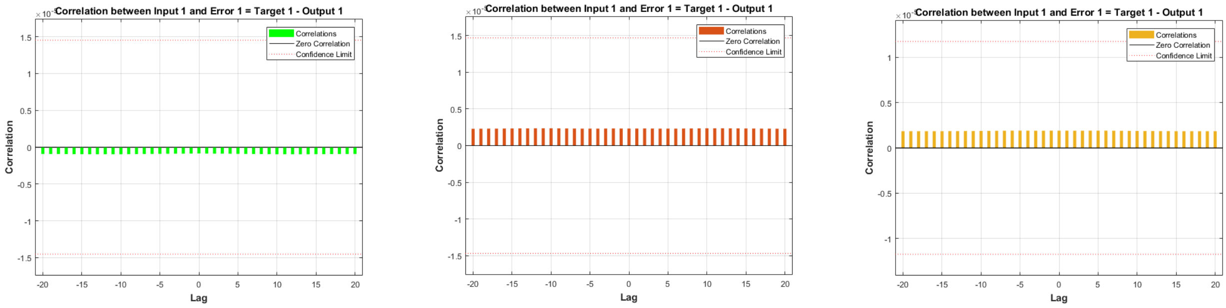

(a) $S(t)$ (b) $L(t)$ (c) $R(t)$

Figure 20. Input error correlation plots for all three epidemiological classes under Scenario 2 ($R_0 > 1$).

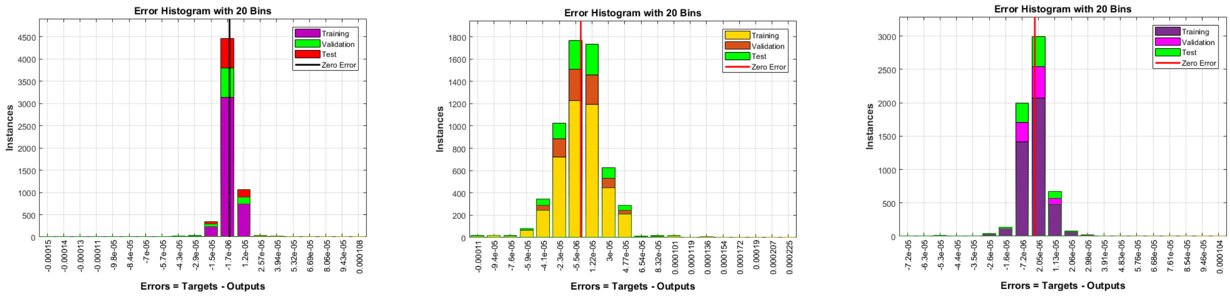

(a) $S(t)$ (b) $L(t)$ (c) $R(t)$

Figure 21. Error histogram plots for all three epidemiological classes under Scenario 1 ($R_0 < 1$).

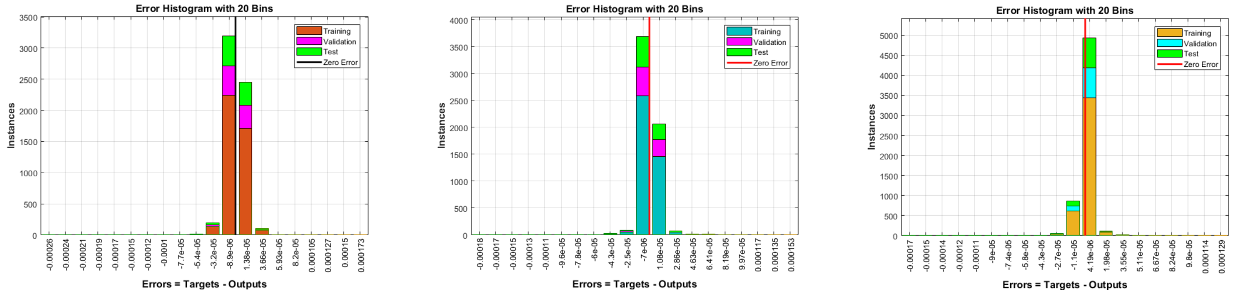

(a) $S(t)$ (b) $L(t)$ (c) $R(t)$

Figure 22. Error histogram plots for all three epidemiological classes under Scenario 2 ($R_0 > 1$).

The regression analysis for the mumps viral model in Scenario 1 ($R_0 < 1$) and Scenario 2 ($R_0 > 1$), across all three classes, $S(t)$, $L(t)$, and $R(t)$, is presented in Figures 23 and 24, respectively. This analysis underscores the importance of forecasting, yielding a correlation coefficient R value approaching 1, indicating the model's success in identifying the underlying data patterns. This correlation reflects the alignment between the model's predictions and the actual observations, confirming the accuracy and reliability of the forecasts.

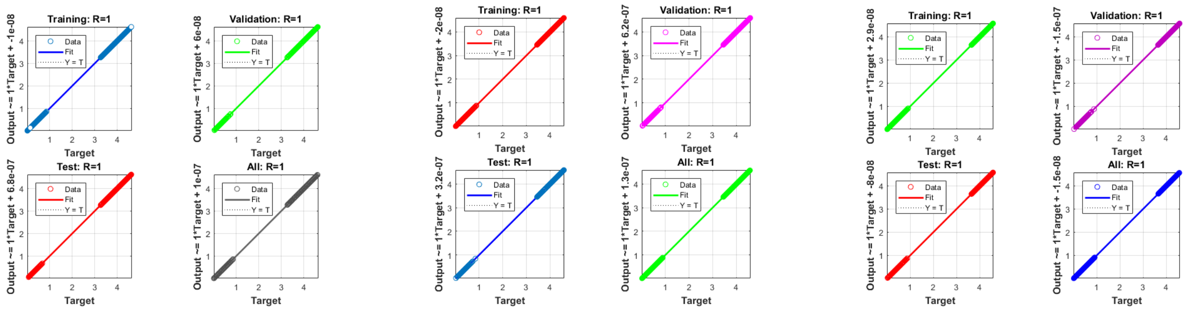

(a) $S(t)$ (b) $L(t)$ (c) $R(t)$

Figure 23. Regression analysis plots for all three classes under Scenario 1 ($R_0 < 1$).

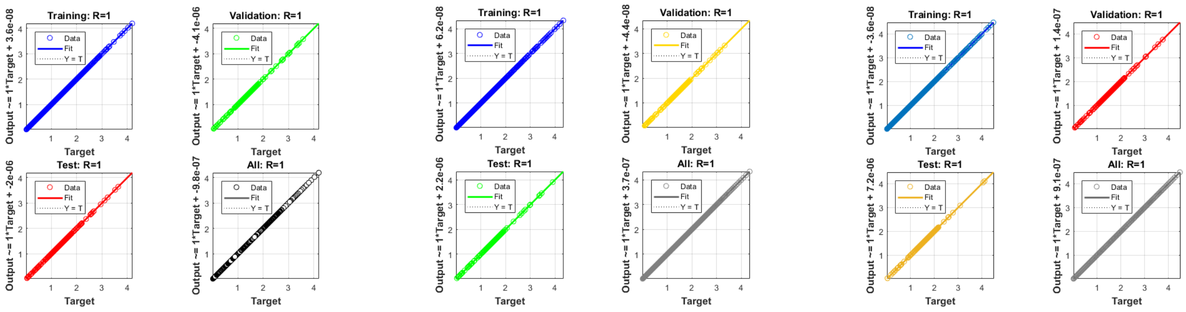

(a) $S(t)$ (b) $L(t)$ (c) $R(t)$

Figure 24. Regression analysis plots for all three classes under Scenario 2 ($R_0 > 1$).

Figures 25 and 26 present the time series response plots for Scenario 1 ($R_0 < 1$) and Scenario 2 ($R_0 > 1$) across all three classes: $S(t)$, $L(t)$, and $R(t)$. These plots illustrate an even distribution of outputs on both sides of the response curve, with minimal errors observed in the training, testing, and validation subsets. This pattern indicates that the model accurately reflects the data. The graphs provide a comprehensive overview of the ANN's behavior and results across various setups and training algorithms. They also demonstrate how changes in model parameters, such as the number of neurons or layers, impact the model's performance and efficiency. Additionally, these plots track the model's progress throughout the training process, ensuring consistency and convergence over the epochs. The comparison of the current results for the mumps viral model in Scenario 1 ($R_0 < 1$) and Scenario 2 ($R_0 > 1$), using Newton's two-step method, Mittag-Leffler Kernel, and numerical solutions with ten neurons, is displayed in Figures 27 and 28 for all three classes: $S(t)$, $L(t)$, and $R(t)$. The results highlight the reliability and accuracy of the proposed approach, as demonstrated by the close alignment between the current outcomes and the Mittag-Leffler numerical solutions. The proposed method consistently matches the results, establishing it as a dependable, accurate, and effective technique.

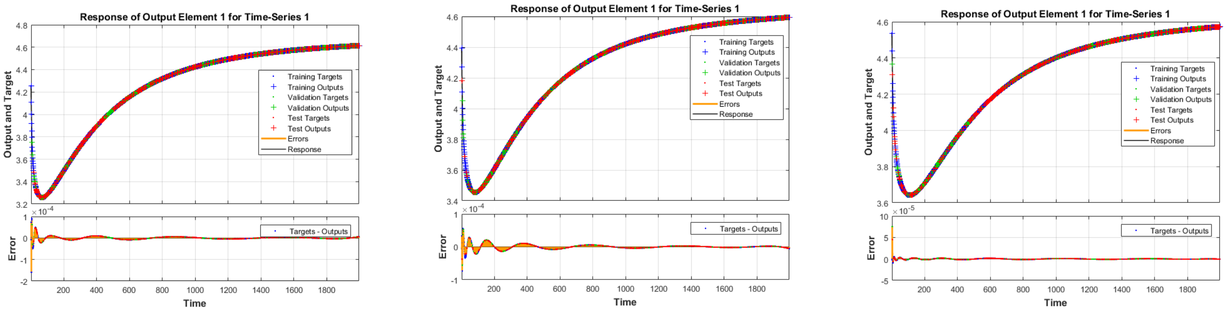

(a) $S(t)$ (b) $L(t)$ (c) $R(t)$

Figure 25. Time series outcomes for all three classes under Scenario 1 ($R_0 < 1$).

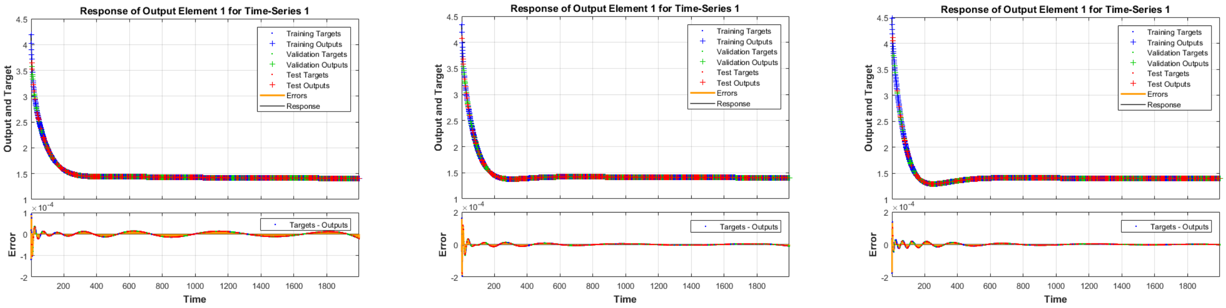

(a) $S(t)$ (b) $L(t)$ (c) $R(t)$

Figure 26. Time series outcomes for all three classes under Scenario 2 ($R_0 > 1$).

Further evaluation of the ANN results is conducted using the absolute error metric for the mumps virus model in both scenarios. The numerical results of solving the fractional-order mumps virus model was obtained using the process of a sigmoid-based neural network. The overlapping of the outcomes is observed for each class of the mumps virus model. The precisely identical results designate the correctness of the designed nonlinear sigmoid basis neural network procedure for solving the nonlinear mumps virus model. The corresponding results for Scenario 1 ($R_0 < 1$) and Scenario 2 ($R_0 > 1$) are shown in Figures 27 and 28, respectively. The results for all three classes, $S(t)$, $L(t)$, and $R(t)$, reveal that the maximum and minimum absolute error values fall within the range of approximately 10^{-2} to 10^{-11}, indicating negligible discrepancies between predicted and actual results values.

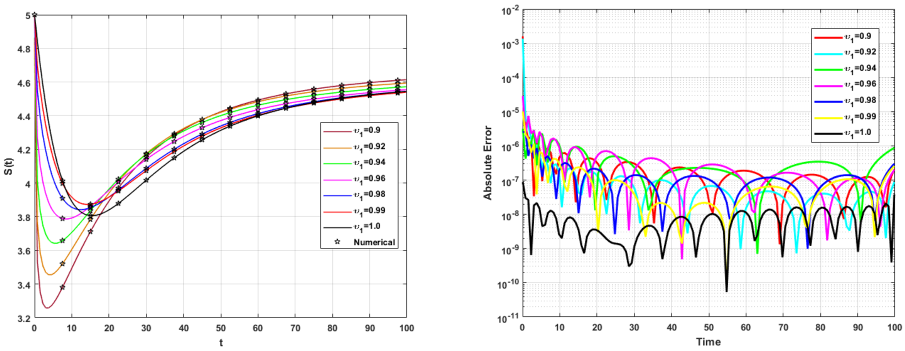

(a) $S(t)$ (b) $S(t)$

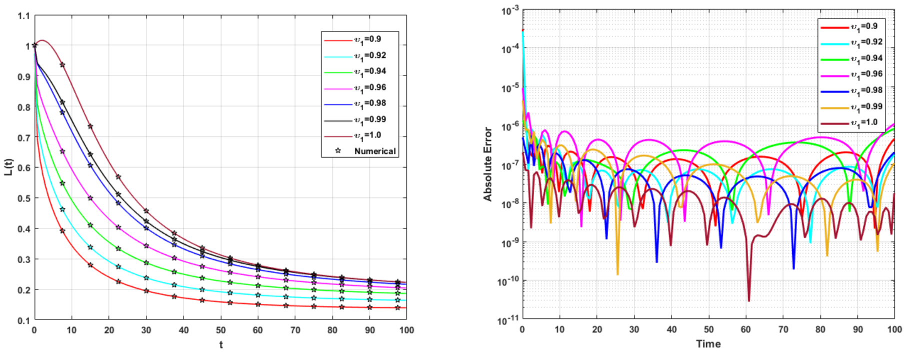

(c) $L(t)$ (d) $L(t)$

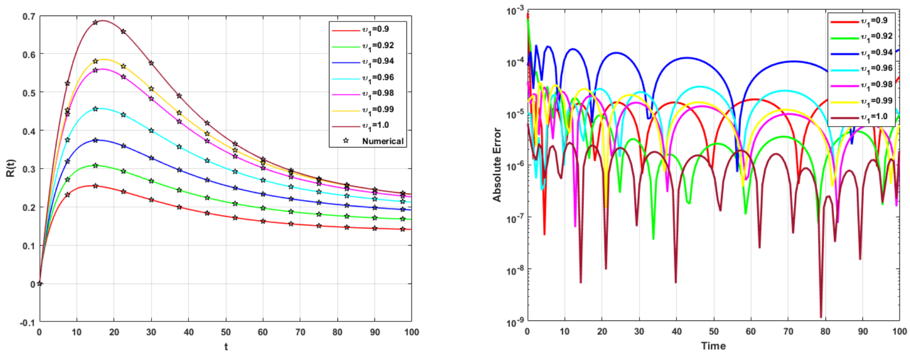

(e) $R(t)$ (f) $R(t)$

Figure 27. Comparison of the errors corresponding to various fractal fractional-orders ν_1 under Scenario 1 ($R_0 < 1$) for the model (2.3).

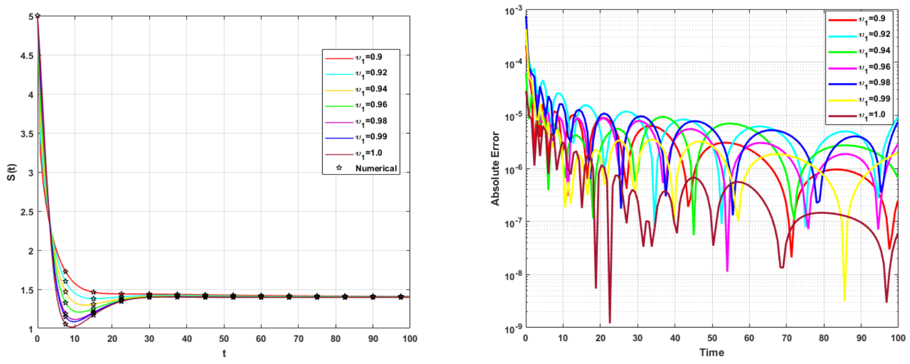

(a) $S(t)$ (b) $S(t)$

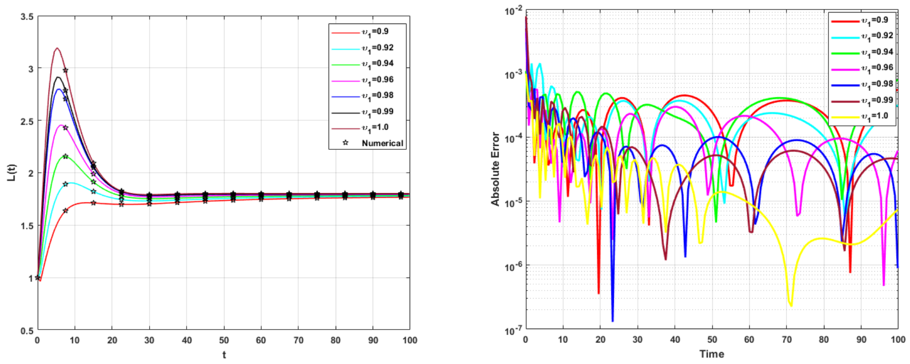

(c) $L(t)$ (d) $L(t)$

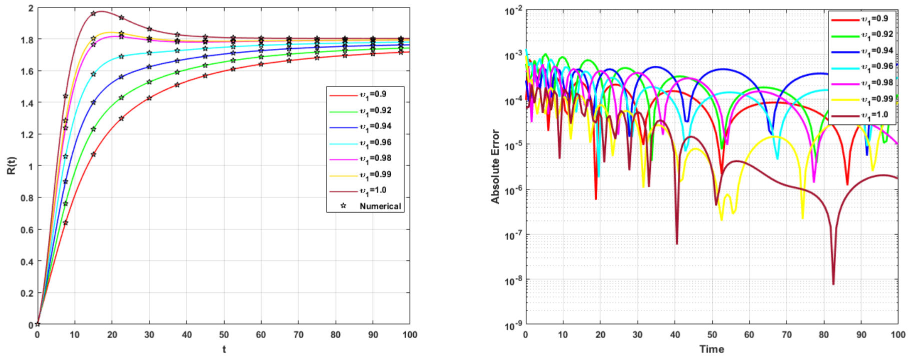

(e) $R(t)$ (f) $R(t)$

Figure 28. Comparison of the errors corresponding to various fractal fractional-orders ν_1 under Scenario 2 ($R_0 > 1$) for the model (2.3).

The comparison of population simulation results in Figure 29 shows that in Scenario 1 ($R_0 < 1$), the mumps virus has stopped spreading, and the proposed method closely matches the actual results. Conversely, in Scenario 2 ($R_0 > 1$), the virus keeps spreading, and the model's predictions remain closely aligned with the observed data. These results highlight the importance of isolating infected individuals to prevent further transmission, which remains one of the most effective strategies for controlling mumps outbreaks. Our ANN evaluation results, presented using the absolute error metric, confirm the effectiveness of the proposed techniques in both scenarios, as shown in Figure 29. Both scenarios of the mumps virus model produce very similar outcomes. The identical results confirm the accuracy of the nonlinear sigmoid basis neural network method for solving the nonlinear mumps virus model.

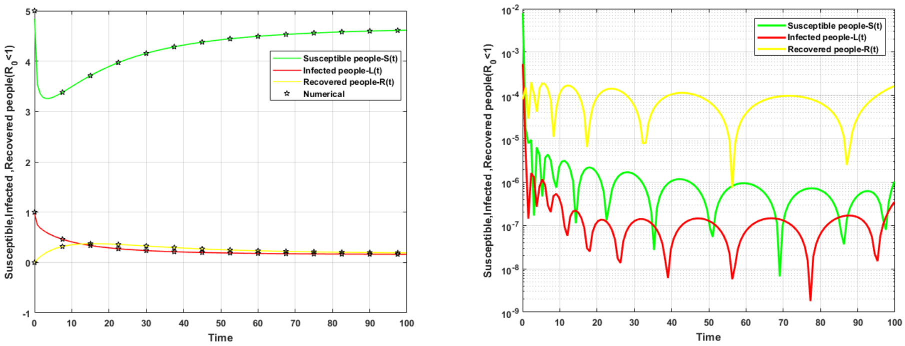

(a) $R_0 < 1$ (b) $R_0 < 1$

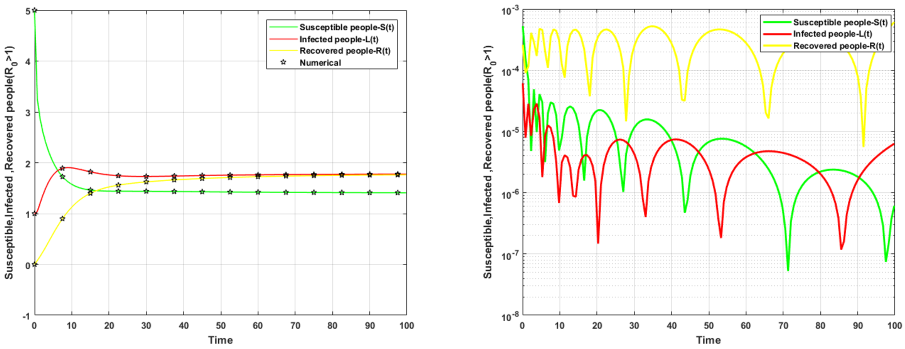

(c) $R_0 > 1$ (d) $R_0 > 1$

Figure 29. Comparison of the simulation results for the S, L, and R populations under both $R_0 < 1$ and $R_0 > 1$ for the model (2.3).

The outcomes mentioned above are further assessed using a variety of evaluation metrics, including MSE, RMSE, MAE, R^2, and $1 - R^2$, with results summarized in Tables 3–6 for all three classes under Scenario 1 ($R_0 < 1$) and Scenario 2 ($R_0 > 1$). These results demonstrate the advantages of using ANN to enhance accuracy in predicting mumps spread. It is clear that near-perfect modeling outcomes are achieved across all performance metrics, and these statistical analyses demonstrate that well-constructed ANNs, simulations, and computational approaches can effectively process both numerical and experimental data. These findings confirm the models' accuracy and encourage innovation in creating systems that can identify complex patterns within intricate datasets. Intelligent computing has great potential to tackle real-world issues, such as disease control.

Table 3. Outcomes of ANN under Scenario 1 ($R_0 < 1$).

Class	Mean square error		Performance	Mu	Gradient	Epochs	Time
	Training	Testing					(sec.)
$S(t)$	6.69E-11	6.62E-11	6.96E-11	1.00E-08	9.95E-08	220	5
$L(t)$	7.35E-11	1.55E-10	8.99E-11	1.00E-08	9.98E-08	247	5
$R(t)$	1.98E-12	5.62E-12	1.06E-11	1.00E-08	9.94E-08	276	6

Table 4. Outcomes of ANN under Scenario 1 ($R_0 < 1$).

Class	MSE	MAE	RMSE	R^2	$1 - R^2$
$S(t)$	6.96E-11	8.6754E-08	8.3427E-06	0.9999	1.4271E-09
$L(t)$	8.99E-11	7.1240E-09	9.4816E-06	0.9999	1.0789E-09
$R(t)$	1.06E-11	1.7717E-08	3.2558E-06	0.9999	1.8811E-10

Table 5. Outcomes of ANN under Scenario 2 ($R_0 > 1$).

Case	Mean square error		Performance	Mu	Gradient	Epochs	Time
	Training	Testing					(sec.)
$S(t)$	1.82E-10	1.61E-10	2.41E-10	1.00E-08	9.92E-08	458	10
$L(t)$	9.29E-11	1.53E-10	1.13E-10	1.00E-08	9.79E-08	335	108
$R(t)$	5.33E-11	5.57E-11	3.21E-11	1.00E-08	9.99E-08	909	19

Table 6. Outcomes of ANN under Scenario 2 ($R_0 > 1$).

Class	MSE	MAE	RMSE	R^2	$1 - R^2$
$S(t)$	2.41E-10	8.7979E-09	1.5524E-05	0.9999	8.4144E-09
$L(t)$	1.13E-10	2.0930E-09	1.0630E-05	0.9999	3.1519E-10
$R(t)$	3.21E-11	5.8242E-10	5.6657E-06	0.9999	1.2691E-09

Integrating numerical modeling with experimental data provides exceptional accuracy in simulating, predicting, and analyzing disease behavior. This computational strategy delivers crucial insights for understanding, preventing, and managing epidemics, effectively connecting theoretical models with real-world health measures. These methods are essential for driving scientific progress, informing public health policies, and enhancing global health outcomes. All performance metrics validate the use of ANNs, as they reliably show precision in analyzing our fractional mumps viral model.

9. Conclusions

The transmission dynamics of the mumps virus have been more effectively understood through a novel nonlinear compartmental model, in which each of the three components operates independently within the proposed framework. The model accounts for the numerous infections and fatalities associated with the virus by addressing disease progression and incorporating individual replacement mechanisms. By integrating mathematical modeling that captures both rapid and slow disease progression cases, the model allows for evaluation of the mumps virus's impact on individuals and communities within any given country. Furthermore, essential mathematical techniques, such as artificial neural networks (ANNs), have been utilized to perform computations within the fractal fractional-order framework.

The fractional-order differential equations governing the model are analyzed for well-posedness to ensure both mathematical rigor and robustness. Ulam-Hyers (UH) stability analysis further confirms the stability of the fractional-order mumps model under therapeutic interventions. The existence and positivity of solutions are guaranteed by applying the Banach fixed-point theorem from nonlinear functional analysis. Comprehensive quantitative and qualitative analyses have been carried out to verify the equilibrium states of the proposed fractional-order mumps viral model.

An advanced numerical method is employed to analyze the epidemic dynamics of mumps, effectively capturing the behavior of such outbreaks. A derivative operator with a nonsingular, nonlocal kernel is utilized to enhance the model's accuracy. The results demonstrate that during the decay phase, particularly at lower fractional orders, the model maintains both effectiveness and consistency with outcomes observed during the growth phase. These findings highlight the critical role of fractional-order parameters in simulations, offering a more realistic and nuanced representation of disease dynamics.

In comparison to traditional methods, the following statements underscore the capability of ANNs to capture complex patterns in the dynamics of mumps virus transmission, offering valuable insights into its spread and behavior.

- ANNs have demonstrated significant potential in modeling and managing human infectious diseases. By leveraging advanced computational techniques, ANNs can simulate and analyze infection dynamics within patient populations, presenting a transformative opportunity for the integration of artificial intelligence in healthcare.
- The accuracy of the proposed model has been validated through comparisons with established benchmarks. These comparisons confirm the precision and robustness of ANNs in modeling and analyzing dynamic behaviors, thereby demonstrating their reliability for the systems under investigation.
- The performance and reliability of ANNs are evaluated using advanced validation metrics, including correlation coefficients, mean squared error (MSE), error histograms, regression diagnostics, time-series analysis, and input-residual cross-correlation. Together, these metrics establish a robust framework for assessing the precision, stability, and predictive effectiveness of the model.
- A reduction in MSE signifies enhanced predictive accuracy, underscoring the effectiveness of the model. The results demonstrate that a well-designed ANN can reliably forecast the dynamic behavior of the mumps virus with minimal errors. The near-zero absolute error further highlights the model's precision in minimizing deviations from observed data, reinforcing its suitability for accurate epidemiological prediction.

These findings confirm that the ANN technique yields accurate and consistent predictions, outperforming traditional methodologies. As such, the ANN framework emerges as a powerful tool in predictive modeling, demonstrating significant potential to surpass conventional approaches in both precision and reliability.

Based on the results obtained, our forthcoming research and applications include simulations for several of the most dangerous viral infections, including those due to the latest COVID variants. Decent mathematical analysis and deep learning strategies will be explored and developed.

Author contributions

I-Hong Lee: Collecting experimental data and completing underlying analysis; Sana Ullah Saqib: For preparing the original manuscript in a collaborative study, creating computational software; Qin Sheng: For contributing to the modeling investigation, reviewing analysis, reviewing and fine-tuning drafts of the paper; Yin-Tzer Shih: For initiating the research topic, procedure, and conceptualization, as well as for supervising, editing, reviewing, and refining the investigations. All authors have read and approved the final version of the manuscript for publication.

Use of Generative-AI tools declaration

The authors declare that they have not used Artificial Intelligence (AI) tools in the creation of this article.

Acknowledgments

The third author thanks the National Science Foundation (Grant No. DMS-2318032) and the Simons Foundation (Grant No. MPS-1001466), USA, for their support. The fourth author would like to acknowledge the support from the National Science and Technology Council (NSTC), Taiwan, through the NSTC project under Grant No. NSTC 114-2115-M-005-002-NY2.

Conflict of interest

All authors declare no conflicts of interest in this paper.

References

1. WHO. *Deafness and hearing loss* (updated 26 February 2025). Available from: `https://www.who.int/news-room/fact-sheets/detail/deafness-and-hearing-loss`.
2. F. Kouilily, F. Z. Aboulkhouatem, N. Yousfi, N. Achtaich, M. El Khasmi, Modeling the social and epidemiological causes of hearing loss, *Rev. Mex. Ing. Bioméd.*, **39** (2018), 248–258.
3. K. S. Nisar, M. Farman, Analysis of a mathematical model with hybrid fractional derivatives under different kernels for hearing loss due to mumps virus, *Int. J. Model. Simul.*, 2024. https://doi.org/10.1080/02286203.2024.2322361
4. F. Kouilily, F. E. Aboulkhouatem, N. Yousfi, M. El Khasmi, N. Achtaich, Mathematical model of hearing loss caused by viral infection, *Rev. Afr. Rech. Inform. Math. Appl.*, 2018.
5. J. Strachan, Mathematical model of hearing loss due to viral infection, *Fla. Sci.*, **85** (2022), 64.

6. W. Al-Sadi, Z. Wei, I. Moroz, A. Alkhazzan, Existence and stability of solution in Banach space for an impulsive system involving Atangana–Baleanu and Caputo–Fabrizio derivatives, *Fractals*, **31** (2023), 2340085. https://doi.org/10.1142/S0218348X23400856
7. W. Al-sadi, Z. Wei, T. Q. S. Abdullah, A. Alkhazzan, J. F. Gómez-Aguilar, Dynamical and numerical analysis of the hepatitis B virus treatment model through fractal–fractional derivative, *Math. Meth. Appl. Sci.*, **48** (2025), 639–657. https://doi.org/10.1002/mma.10348
8. F. Arif, S. U. Saqib, Y. T. Shih, Y. T. Kausar, SEIR-VQ model for the NB.1.8.1 COVID-19 variant: Mathematical analysis and numerical simulations, *AIMS Mathematics*, **10** (2025), 18024–18054. https://doi.org/10.3934/math.2025803
9. A. G. Schilder, L. Y. Chong, S. Ftouh, M. J. Burton, Bilateral versus unilateral hearing aids for bilateral hearing impairment in adults, *Cochrane Database Syst. Rev.*, **12** (2017), CD012665. https://doi.org/10.1002/14651858.cd012665.pub2
10. M. R. Thulasiram, J. M. Ogier, A. Dabdoub, Hearing function, degeneration, and disease: Spotlight on the stria vascularis, *Front. Cell Dev. Biol.*, **10** (2022), 841708. https://doi.org/10.3389/fcell.2022.841708
11. B. Challa, J. Kethar, Connecting hearing loss: Causes, treatments, and prevention, *J. Stud. Res.*, 11 (2022). https://doi.org/10.47611/jsrhs.v11i4.3717
12. Y. J. Zhou, J. Yu, Y. Z. Wu, L. Tian, Z. Han, J. Wang, et al., The potential dysfunction of otolith organs in patients after mumps infection, *PLoS One*, **12** (2017), e0181907. https://doi.org/10.1371/journal.pone.0181907
13. M. Farman, A. Hasan, M. Sultan, A. Ahmad, A. Akgül, F. Chaudhry, et al., Yellow virus epidemiological analysis in red chili plants using Mittag-Leffler kernel, *Alexandria Eng. J.*, **66** (2023), 811–825. https://doi.org/10.1016/j.aej.2022.10.064
14. C. Xu, M. Farman, A. Hasan, A. Akgül, M. Zakarya, W. Albalawi, et al., Lyapunov stability and wave analysis of Covid-19 omicron variant of real data with fractional operator, *Alexandria Eng. J.*, **61** (2022), 11787–11802. https://doi.org/10.1016/j.aej.2022.05.025
15. A. Atangana, Modelling the spread of COVID-19 with new fractal-fractional operators: Can the lockdown save mankind before vaccination? *Chaos Solitons Fractals*, **136** (2020), 109860. https://doi.org/10.1016/j.chaos.2020.109860
16. H. Mohammadi, S. Kumar, S. Rezapour, S. Etemad, A theoretical study of the Caputo-Fabrizio fractional modeling for hearing loss due to mumps virus with optimal control, *Chaos Solitons Fractals*, **144** (2021), 110668. https://doi.org/10.1016/j.chaos.2021.110668
17. J. K. Asamoah, E. Addai, Y. D. Arthur, E. Okyere, A fractional mathematical model for listeriosis infection using two kernels, *Decis. Anal. J.*, **6** (2023), 100191. https://doi.org/10.1016/j.dajour.2023.100191
18. S. U. Saqib, U. Farooq, N. Fatima, Y. T. Shih, A. Mir, L. Kolsi, Novel recurrent neural networks for efficient heat transfer analysis in radiative moving porous triangular fin with heat generation, *Case Stud. Therm. Eng.*, **64** (2024), 105516. https://doi.org/10.1016/j.csite.2024.105516

19. M. Shoaib, S. U. Saqib, M. A. Z. Raja, K. S. Nisar, Intelligent computing Levenberg Marquardt technique for MHD hybrid nanofluid radiative-dissipative flow along stretched surface under influence of slip and convective conditions, *Waves Random Complex Media*, 2022. https://doi.org/10.1080/17455030.2022.2123572

20. M. W. Anjum, S. U. Saqib, Y. T. Shih, I. Ul Hassan, Adnan, I. H. Jaghdam, et al., Application of Kolmogorov-Arnold network (KAN) for solitary-Peakon investigation of Lax model, *Case Stud. Therm. Eng.*, **73** (2025), 106537. https://doi.org/10.1016/j.csite.2025.106537

21. I. Goodfellow, Y. Bengio, A. Courville, *Deep learning*, MIT Press, 2016.